micromachines

MDPI

Article

Influence of Micro-Textured Carbide Tools on Ti-Grade-9 Alloy Turning: Machinability Assessment and Multi-Response Hybrid Optimization

Abhijit Samant, Ramanuj Kumar*, Ashok Kumar Sahoo and Amlana Panda

MRL Lab, School of Mechanical Engineering, Kalinga Institute of Industrial Technology (KIIT) Deemed to be University, Bhubaneswar751024, Odisha, India; erabhijitsamant@gmail.com (A.S.); aksahoofme@kiit.ac.in (A.K.S.); amlana.pandafme@kiit.ac.in (A.P.)

* Correspondence: ramanujkumar22@gmail.com

Abstract

Titanium-grade 9 (Ti-3Al-2.5V) is a lightweight alloy with high strength and corrosion resistance; however, its low thermal conductivity and chemical reactivity make machining challenging, resulting in high cutting temperature, high tool wear, poor surface quality, and high energy consumption. This study investigates the influence of laser-induced micro-textured carbide tools on the machinability of titanium-grade-9 alloy during CNC turning. Micro-textures were fabricated using a fiber laser machine on the rake and flank faces of the cutting tool. The experiments were designed using an L_{18} orthogonal array with four control factors, namely tool type (*Tt*), cutting speed (*v*), feed (*f*), and depth of cut (*d*). The tool type factor comprised three configurations: untextured tool (T1), grooved texture on both rake and flank face (T2), and dotted texture on the rake face combined with grooved texture on the flank face (T3). The machinability and texture tools performance were analyzed using results of surface roughness, cutting temperature, tool wear, and cutting-power consumption. T2 exhibited the best performance, while abrasion and adhesion were the most dominant forms of wear identified. CRITIC-MARCOS optimization identified tool type T2, a cutting speed of 80 m/min, a feed of 0.06 mm/rev, and a depth of cut of 0.2 mm as optimal parameters.

Keywords: titanium-grade 9; micro-texture; grooved texture; dotted texture; surface roughness; cutting temperature; tool wear; cutting power consumption; CRITIC-MARCOS; hybrid optimization

Academic Editors: Guochao Li, Reza Teimouri, Zhaoju Zhu and Youqiang Xing

Received: 8 September 2026
Revised: 27 October 2026
Accepted: 28 October 2026
Published: 30 October 2026

Copyright: © 2026 by the authors. Licensee MDPI, Basel, Switzerland. This article is an open access article distributed under the terms and conditions of the Creative Commons Attribution (CC BY) license.

1. Introduction

Metal machining is an essential process in the manufacturing sector for converting engineering materials into useful components for various industrial applications. Engineering materials such as titanium alloys, nickel-based alloys, and hardened steels come under the category of difficult-to-machine materials and are widely used in various core industries. The major challenges associated with machining these materials include the generation of high cutting temperatures, high cutting loads, and increased strain hardening, resulting in accelerated tool wear, reduced tool life, poor surface finish, and compromised surface integrity [1–3]. These challenges adversely affect the machining efficiency of difficult-to-machine materials.

To improve the cutting efficiency of these materials, the role of cutting tools is crucial and important. In the past literature, many tool materials with distinct tool geometries were implemented for machining these materials. Micro-texturing on the tool surface improves the tribological, optical, biological, and wetting properties of the tool surface to meet the desired needs [1]. Textured surfaces have shown significant benefits in terms of anti-adhesion, anti-fouling performance, reduced corrosion, acting as a coolant reservoir, and self-cleaning properties [1,4–6].

In practice, a textured surface reduces the direct contact area between the tool and the chip, thereby reducing frictional resistance, cutting temperature, and cutting forces [7]. Moreover, the texture features can act as reservoirs for detached chips, thereby reducing chip accumulation in the cutting zone [1]. In addition, the micro-textured pattern increases the effective heat-transfer area between the tool and the chip and between the tool and the workpiece, potentially enhancing heat dissipation to the surroundings and helping to control cutting temperatures [8]. As a result, tool life and surface finish may be improved during the cutting process.

The application of texture tools in the machining process aligns with the concept of green machining, showing the importance of advanced manufacturing technology in environmental protection and sustainable growth [9]. For machining activities, the use of textured patterns and texturing techniques plays a vital role in achieving the desired cutting efficiency. In the literature, many textured patterns, namely grooves, waves, pits, diamond, zigzag, volcano, and mixed patterns, were developed and applied for machining [9–11]. Moreover, these patterns on the tool rake and flank surfaces were created by electrical-discharge machining, photolithography, and laser processing.

Machining of Ti alloys is challenging due to their poor thermal conductivity and high strain hardening [9]. Textured cutting tools showed potential benefits in machining titanium alloys. According to Sristi and Zaman [12], surface-textured cutting tools have emerged as a promising sustainable solution to reduce cutting fluid consumption while improving lubrication, chip flow, and machining efficiency. Sergey Grigoriev et al. [13] have investigated micro- and nano-texturing on the rake face of cutting tools using features such as grooves, dimples, pits, and chevron patterns. These textures reduce the tool–chip contact area, improve lubrication, facilitate chip evacuation, and minimize friction and tool wear, thereby enhancing tool life and surface quality. Zhang et al. [14] utilized textured cutting tools in machining hardened steel and found that textured coated tools reduced cutting force, cutting temperature, friction coefficient, and tool wear compared to conventional cutting tools. Fernandez et al. [15] reviewed the application of laser surface texturing for improving the machinability of the Ti-6Al-4V alloy. It was concluded that the laser-textured cutting tools enhance tribological performance by reducing friction, improving heat dissipation, and extending tool life. In another study [16], the effect of surface-texture orientation on tribological behavior during the interaction between WC-Co and Ti-6Al-4V was studied. Under lubricated conditions, the perpendicular texture was found to be more advantageous than the horizontal and 45° texture orientations, whereas severe adhesion was observed under dry conditions. Elias et al. [17] utilized the micro-indentation method for creating texture design on cutting tools. Further, the textured tools were utilized in turning Ti-6Al-4Valloy under minimum Quantity Lubrication (MQL). Experimental results demonstrated an improvement in machining performance including reduction of approximately 21% in cutting force, 7% in cutting temperature, 19% in flank wear, and 6% in surface roughness compared to non-textured tools. According to Alok et al. [18], surface texturing on both rake and flank faces of tools exhibited considerable decrease in the tool wear and extending tool life. The integration of textured cutting tools with sustainable cooling and lubrication techniques has demonstrated significant potential for improving machining efficiency, surface qual-

ity, and environmental sustainability. Zhang et al. [19] proposed a novel hexagonal micro-textured PCBN cutting tool to improve turning performance. Using finite-element simulations and experimental validation, they found that micro-textures on both the rake and flank faces, combined with solid lubricants, reduced cutting forces by 3–7%, lowered friction and cutting temperature, improved workpiece surface finish, and enhanced tool-wear resistance. Their study demonstrated that properly designed dual-face micro-texture can significantly improve the machining performance and service life of PCBN cutting tools. Mallikarjuna et al. [20] investigated the performance of a textured cutting tool during MQL turning of EN24 alloy steel. The textured tool was compared with a conventional untextured tool by evaluating cutting temperature, surface roughness, tool wear, and chip morphology. The results showed that the textured tool reduced cutting temperature, rake wear, flank wear, and surface roughness, leading to improved machining performance. The study concluded that combining surface texturing with MQL effectively enhances lubrication, minimizing adhesion and extending tool life.

Multi-response optimization (MRO) in machining research is essential for determining optimum machining conditions while simultaneously considering multiple performance characteristics. With recent advancement in MRO for machining processes, hybrid multi-criteria decision-making (MCDM) frameworks have gained increasing attention. In a hybrid MCDM framework, an objective weighting method is first employed to determine the relative importance of multiple responses, followed by a separate MCDM method to rank the experimental alternatives. Vijayanath et al. [21] integrated CRITIC with COPRAS for multi-response optimization. Similarly, Ramai et al. (2025) [22] implemented a hybrid Entropy-MOORA approach for multi-response machining optimization. Sultana and Dhar [23] employed the CRITIC-COPRAS, CRITIC-COCOSO, CRITIC-TOPSIS, and CRITIC-ARAS hybrid frameworks for the optimization of end milling of Ti-grade-5 alloy. The sensitivity analysis of the resulting optimal solutions demonstrated that combining an objective weighting method with an independent ranking approach provides a systematic framework for solving multi-response optimization problems. Kavimani et al. [24] integrated CRITIC with WASPAS for multi-response optimization. Uyala et al. [25] employed several objective weighting techniques, including CRITIC, MEREC, and standard deviation (SD), in combination with the MARCOS method for optimizing EDM process parameters. Their findings recommended the use of either SD or CRITIC-based weighting in combination with MARCOS to optimize other machining responses. Pradhan et al. [26] employed the MARCOS technique for machining parameter optimization, demonstrating its applicability to manufacturing processes involving multiple performance characteristics. Additionally, Pendo Khare et al. [27] conducted a comprehensive review of parametric optimization in EDM processes and concluded that integrating different weighting and ranking methods is a recognized strategy for systematically addressing conflicting machining responses.

Based on the literature reviewed, the textured cutting tools have demonstrated considerable potential for improving cutting forces, cutting temperature, tool wear, and surface finish during machining of titanium alloys. However, a comprehensive investigation of their combined effects remains limited. Moreover, very few studies have reported the use of cutting tools textured on both the rake and flank surfaces for machining titanium alloys. In addition, dotted and grooved patterns produced by the laser texturing method have rarely been investigated simultaneously. Therefore, the influence of texture characteristics in combination with machining parameters on multiple machining responses under dry machining conditions remains insufficiently established. Although several hybrid MCDM frameworks have recently been applied to machining optimization, the application of the CRITIC–MARCOS framework to the machining of titanium-grade-9 alloy using textured cutting tools remains unexplored. Therefore, an inte-

grated, objective, and data-driven CRITIC–MARCOS framework is needed to determine the relative importance of the machining parameters and optimize multiple machining responses simultaneously.

In view of the identified research gaps, the present study developed two distinguished texturing patterns (grooves and dotted) on the rake surface of the cutting tool, together with vertical grooves on the flank surface. The developed texture tools, together with an untextured tool were employed for machining titanium-grade-9 alloy using a three-axis CNC lathe under dry machining conditions. The effects of the tool-texturing patterns and cutting parameters on the selected machining responses were systematically investigated. Furthermore, a novel CRITIC-MARCOS hybrid MRO framework was employed to objectively determine the relative importance of the machining responses and subsequently identify the optimum combination of cutting parameters and tool-texturing patterns to achieve balanced machining performance.

2. Materials and Methods

The machining tests were performed on a 3-axis CNC lathe (Model: DX 200 4A, manufactured and marketed by Jyoti Automation Ltd., Rajkot, Gujarat, India). A cylindrical rod of titanium-grade 9 (Ti-3Al-2.5V) was selected as a workpiece (initial diameter = 50 mm, total length = 150 mm, cutting length = 110 mm, and hardness = 35 HRC) due to its primary applications in aerospace, medical, and marine components. The three different types of uncoated carbide cutting tools (T1 = Untextured; T3 = grooved texture on the rake face and vertical groove on the flank face; and T3 = dotted texture on the rake face and vertical groove on the flank face) were used and taken as an input factor. The texturing on tool surfaces was accomplished by a 20-Watt Fiber-Laser marking machine supplied by Agile Machineries Pvt. Ltd.,Gandhinagar, Gujarat, India. The details of texturing methodology are presented in Figure 1. To create these patterns on both the rake and flank surfaces, the laser power, scanning speed, and frequency were set to 20 W, 200 mm/s, and 20 kHz, respectively. Ten passes were used to create patterns on the tool surfaces. The schematic views of textured tools T2 and T3 are presented in Figures 2 and 3, respectively. For tool T2, the spacing between two consecutive grooves is 0.02 mm, the groove width is 0.03 mm, and the groove depth is 0.02 mm on both the rake and flank surfaces. The orientation of grooves on rake faces is at 45° to the main cutting edge, whereas those on the flank face are vertically oriented. The gap between cutting edge and texturing zone was about 0.5 mm. Similarly, for tool T3, the center-to-center spacing between two consecutive dots is 0.03 mm, the dot diameter is 0.02 mm, and the dot depth is 0.02 mm on the rake surface. On the flank surface of tool T3, the spacing between two consecutive grooves is 0.02 mm, and the groove width is 0.03 mm, with the grooves oriented vertically.The cutting insert (CNMA120408, THM grade) was manufactured by WIDIA (Kennametal Inc., Pittsburgh, PA, USA) and had the following tool geometry: 95° approach angle, 80° included angle, −6° rake angle, and 0.8 mm nose radius. The tool exhibited a 1564 HV microhardness at a 2 Kgf test load, demonstrating its high hardness and potential suitability for machining titanium alloys.

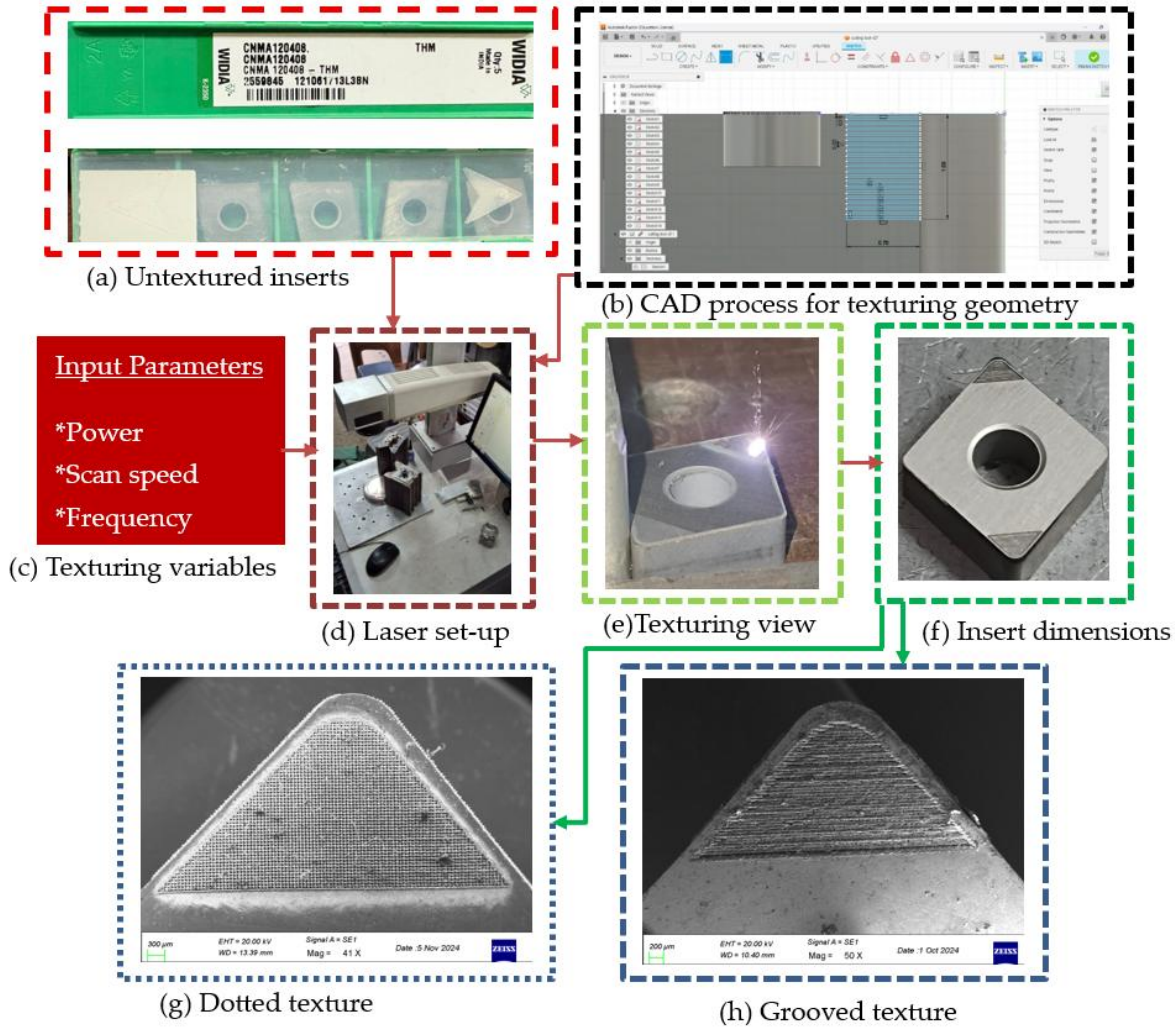


Figure 1. Fiber laser enables texturing on cutting-tool surface (**a**) untextured insert (**b**) CAD process for texturing geometry (**c**) texturing variables (**d**) Laser set-up (**e**) texturing view (**f**) textured insert dimensions (**g**) SEM image of dotted texture (**h**) SEM image of grooved texture. * The figure illustrates the procedure for creating dotted and grooved textures on the surface of carbide cutting-tool inserts using laser texturing.

The experiments were planned to use a Taguchi L_{18} design comprising four factors, each at three levels. The input factors were tool type (Tt = T1, T2, and T3), cutting speed (v = 80, 140, and 200 m/min), feed (f = 0.06, 0.12, and 0.18 mm/rev), and depth of cut (d = 0.1, 0.2, and 0.3 mm). The L_{18} orthogonal array was selected because the experimental study involved four machining factors, each considered at three levels. The L_{18} array provides a systematic and statistically balanced arrangement of factor-level combinations, enabling the individual effects of the selected machining parameters to be evaluated using substantially fewer experimental trials than a full factorial design. A full factorial design for four factors at three levels would require (3^4 = 81) experimental combinations, whereas the L_{18} orthogonal array requires only 18 experimental runs. Therefore, the L18 design was considered appropriate for obtaining information about the main effects of the machining parameters while reducing experimental time, material consumption, and machining cost. Moreover, owing to the limited availability of machining resources, cutting tools, workpiece material, and experimental time, it was not feasible to perform independent machining replicates for each experimental condition. Therefore, each experimental condition was conducted only once according to the selected L_{18} orthogonal array. Although an L_9 orthogonal array could reduce the number of experimental trials, the L_{18}

design was selected to provide a broader experimental dataset for evaluating the influence of the machining parameters and conducting subsequent multi-response optimization. A total of 18 experiments were performed, with each experimental condition tested once. Independent replication was not conducted due to practical constraints associated with machining time, material consumption, and experimental costs. Consequently, the absence of independent replication limits the estimation of pure experimental error and the assessment of run-to-run variability, and this limitation is considered when interpreting the results. Repeated measurements of the same machined specimen were used to assess measurement repeatability; however, these measurements do not constitute independent experimental replications and cannot be used to estimate the variability associated with repeating the machining process under identical conditions. To enhance the reliability and consistency of the measurements, calibrated measuring instruments were used, and a consistent measurement procedure was followed for all experimental conditions. Where applicable, multiple readings were taken for each response, and their average values were used for subsequent analysis. The responses measured were surface roughness (*Ra*), cutting temperature (*T*), flank wear (*VB*), and cutting power consumption (*Cp*). Surface roughness was measured using a portable surface-roughness tester (Model: Siltronic Duo II, Taylor Hobson Ltd., Leicester, UK), and the mean of five measurements was used for analysis. The temperature distribution during the turning of Ti-grade 9 was monitored using a FLIR T540 thermal camera (Teledyne FLIR, Täby, Stockholm, Sweden). The camera was positioned at a fixed distance of 50 ± 5 cm from the cutting zone, with the lens directed towards the visible workpiece surface adjacent to the cutting edge. The emissivity was set to 0.6 for each test. A fixed region of interest (ROI) was selected around the visible tool-workpiece contact region. The maximum temperature within the ROI was recorded for each experimental run. Since the chip may obstruct the tool–workpiece interface, the measured temperature represents the visible surface temperature within the ROI rather than the true interface temperature. The cutting-edge condition was controlled by using a new cutting edge for each experimental run. Therefore, accumulated tool wear from the previous machining operation was avoided, and each experiment was started with an unused cutting edge under the specified cutting conditions. The cutting tool was carefully inspected before each experiment to ensure that there was no visible damage or pre-existing wear on the cutting edge. This approach was followed consistently for all experimental trials to maintain a uniform initial cutting-edge condition and to minimize the influence of accumulated tool wear on the experimental results. Flank wear was evaluated based on the average width of the flank wear land (VB) developed on the tooltip worn region after machining. Flank wear was evaluated based on the average width of the flank wear land (VB) developed in the worn region of the cutting edge after machining. Flank wear was measured using an Olympus STM6 optical microscope equipped with Stream image analysis software (Olympus Corporation, Hachioji, Tokyo, Japan). After each machining run, the cutting tool was carefully removed from the tool holder and cleaned properly to eliminate adhered workpiece material and cutting lubricant residues. The tool was then positioned under the microscope, and the width of the flank wear land was measured at the specified cutting-edge location. The measurements were carried out in accordance with the guidelines of ISO 3685 [28], and the average of five flank wear measurements was recorded for comparison among the different machining runs. Cutting power was recorded using a power and energy meter, capturing the power consumed during CNC lathe operation, including workpiece turning. Surface roughness and flank wear were measured after each run, whereas cutting temperature and power were recorded during machining. X-ray diffraction (XRD) analysis was performed on the finished surfaces corresponding to the minimum and maximum measured *Ra* values. Raman spectroscopy was also

conducted on the worn cutting-tool edge to investigate adhesive wear. Atomic force microscopy (AFM) was used to characterize the surface topography at the nanoscale. ANOVA was performed using Minitab Statistical Software, Version 17. Minitab, Inc.: State College, PA, USA, 2014to evaluate the statistical significance of the input parameters for each response. The significance of each parameter was determined based on its *p*-value. A parameter was considered statistically significant if its *p*-value was less than 0.05, whereas it was considered statistically insignificant if its *p*-value was greater than 0.05. Furthermore, the percentage contribution of each input parameter was calculated by dividing its adjusted sum of squares (Adj SS) by the total adjusted sum of squares and multiplying the result by 100. The validity of ANOVA depends on the residual assumptions, including normality, independence, and constant variance. The absence of independently replicated machining conditions limits the estimation of pure experimental error and, consequently, the strength of the statistical inferences. Therefore, the ANOVA results are interpreted in the context of the limitations of the adopted experimental design. Moreover, to assess the variability associated with the experimental measurements, the standard error (SE) was calculated for each measured response based on five measurement readings. The average standard error values were 0.00889 μm for surface roughness (*Ra*), 0.771 °C for temperature (*T*), 0.00167 mm for tool wear (*VB*), and 0.00632 kW for cutting power (*Pc*). The corresponding 95% confidence interval (CI) half-widths were calculated using the t-distribution for a small sample size, with four degrees of freedom. The resulting half-widths were ±0.02469 μm for *Ra*, ±2.1409 °C for *T*, ±0.00464 mm for *VB*, and ±0.01755 kW for *Pc*. These confidence intervals quantify the uncertainty associated with the average of the five measurement readings for each response. The experimental and measurement setups are illustrated in Figure 4.

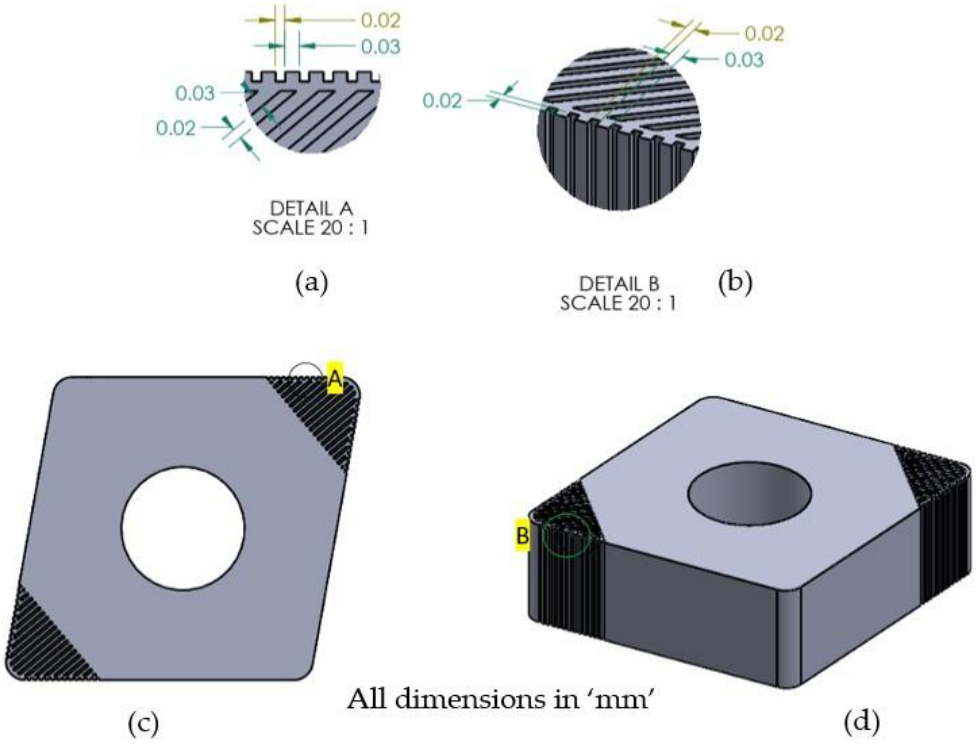


Figure 2. Schematic view of developed groove texture (**a**) cross-sectional (region A) view of texture on rake surface, (**b**) cross-sectional (region B) view of texture on flank surface, (**c**) rake surface, and (**d**) flank surface of cutting tool (T2).

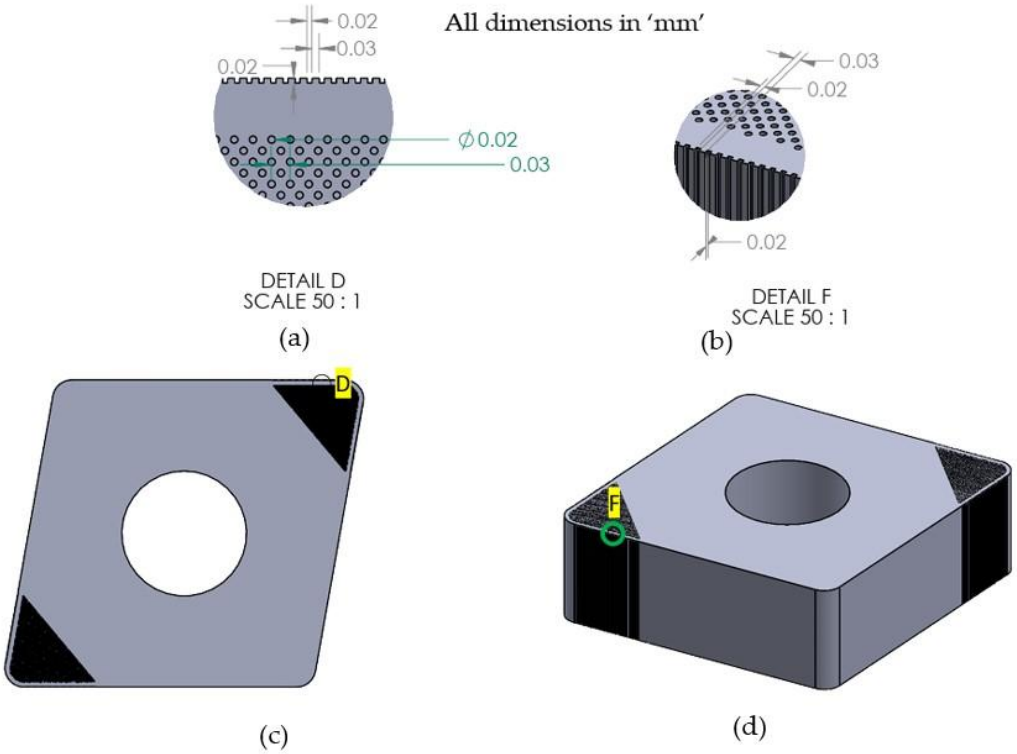


Figure 3. Schematic view of developed dotted texture (**a**) cross-sectional (region D) view of texture on rake surface, (**b**) cross-sectional (region F) view of texture on flank surface, (**c**) rake surface, and (**d**) flank surface of cutting tool (T3).

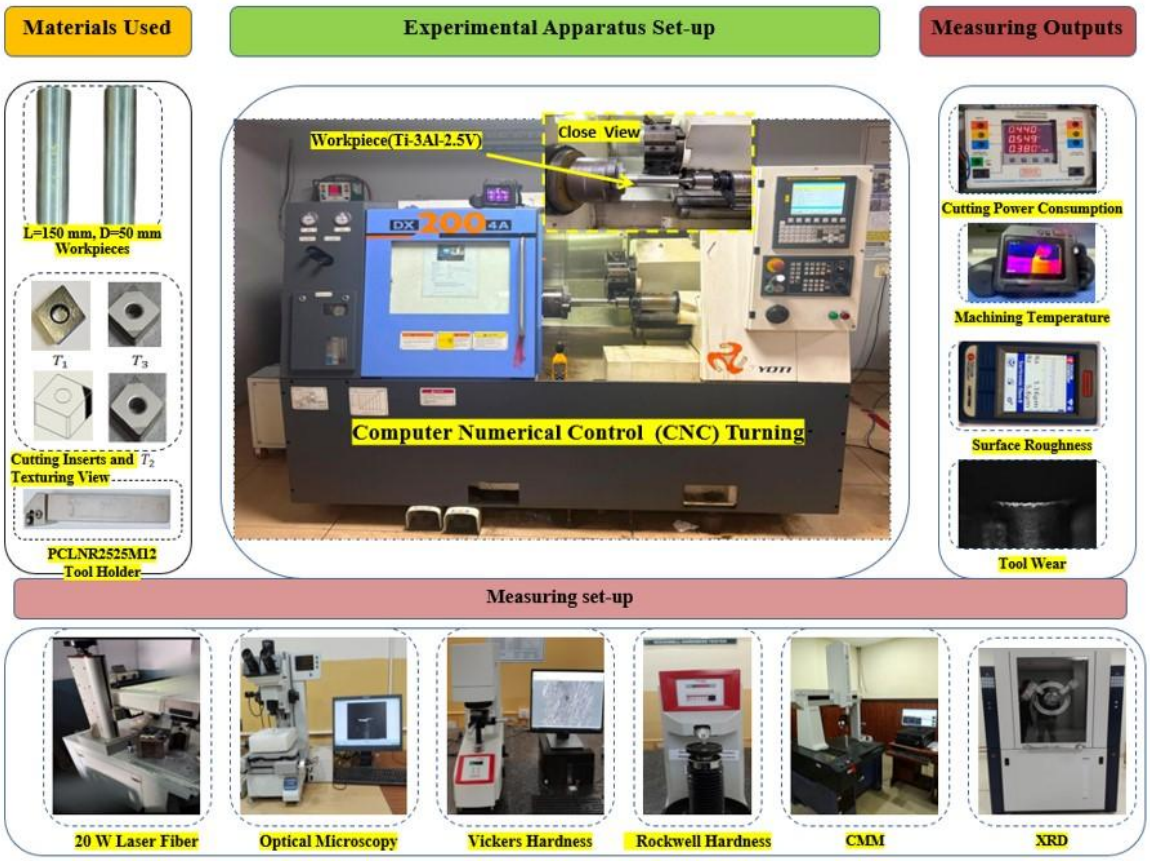


Figure 4. Details of experimental and measurement setups.

2.1. CRITIC-MARCOS Hybrid Optimization Method

In this hybrid methodology, the CRITIC (Criteria Importance Through Intercriteria Correlation) method is used to determine the weight of each response. It is an objective weighting technique that assigns weights to criteria based on their contrast intensity and conflict (intercriteria correlation) in a decision-making problem [29,30]. The weights obtained using the CRITIC method is then integrated into the MARCOS (Measurement of Alternatives and Ranking According to Compromise Solution) method for multi-response optimization [31]. The detailed step-by-step methodology is presented below.

Step 1: Construct the decision matrix

The decision matrix (X_{ij}) was constructed using experimentally measured response data, as expressed in Equation (1).

$$X_{ij} = \begin{bmatrix} x_{11} & \cdots & x_{1l} \\ \vdots & \ddots & \vdots \\ x_{i1} & \cdots & x_{ij} \end{bmatrix} \quad (1)$$

where X_{ij}= value of j^{th} criterion for the i^{th} alternative, i =1, 2, …,18 and j = 1, …,4.

Step 2: Normalize the decision matrix

In the current study, all responses (*Ra*, *T*, *VB*, and *Cp*) are non-beneficial, for which lower values are preferred. Therefore, Equation (2) is used to estimate normalized decision matrix. The normalized values range from 0 to 1.

$$N_{ij} = \frac{x_j{}^{max} - x_{ij}}{x_j^{max} - x_j^{min}} \quad (2)$$

where N_{ij} = normalized value, $x_j{}^{max}$= highest value of criterion j^{th} and x_j^{min} = lowest value of criterion j^{th}.

Step 3: Determine the value of standard deviation of each criterion

The standard deviation quantifies the variability of values for each criterion. Equation (3) is used to calculate the standard deviation of each criterion. A higher standard deviation indicates greater variability among alternatives and, consequently, greater discriminatory power of the criterion.

$$\sigma_{j=}\sqrt{\frac{\sum_{i=1}^{m}(N_{ij} - \bar{N}_j)^2}{m-1}} \quad (3)$$

where $\sigma_{j\,=}$ standard deviation of criterion j, $\bar{N}_j$= average for normalized value of criteria j, and m= total number of alternatives

Step 4: Determine the correlation coefficient matrix

The Pearson correlation coefficient between the $j^{th}$and k^{th} criteriais estimated using Equation (4).

$$C_{jk} = \frac{\sum_{i=1}^{m}(N_{ij} - \bar{N}_j)(N_{ik} - \bar{N}_k)}{\sqrt{\sum_{i=1}^{m}(N_{ij} - \bar{N}_j)^2}\sqrt{\sum_{i=1}^{m}(N_{ik} - \bar{N}_k)^2}} \quad (4)$$

where C_{jk}= Degree of correlation between the j^{th} and k^{th} criteria. The value of the Pearson correlation coefficient ranges from −1 to +1. A value of +1 indicates a perfectly positive linear relationship, 0 indicates no linear correlation, and −1 indicates a perfectly negative linear relationship.

Step 5: Determine the information content of every criterion

The amount of value contained in criterion j^{th} is estimated using Equation (5). The information content depends on the standard deviation of the criteria and its correlation

with other criteria. A higher standard deviation indicates greater discriminatory power, while a lower correlation with other criteria indicates that the criteria provide more unique information. Therefore, criteria with high variability and low redundancy receive higher information content values.

$$\rho_j = \sigma_j \sum_{k=1}^{n} \left(1 - \left(C_{jk}\right)\right) \tag{5}$$

where ρ_j= information content of criterion j, σ_j= standard deviation, and C_{jk}= correlation coefficient.

Step 6: Determine the objective weightage of individual criteria

The CRITIC weightage for each criterion is estimated using Equation (6). The summation of all criteria weights should equal 1. Further, these estimated weights are used as input weights in the MARCOS method.

$$w_j = \frac{\rho_j}{\sum_{j=1}^{n} \rho_j} \tag{6}$$

where $w_j$is the weight of the j^{th} criteria, and n represents the total number of criteria.

Step 7: Construct the extended decision matrix

In this step, two additional alternatives are introduced in an already constructed decision matrix in step 1. For the non-beneficial criterion, the first alternative is the ideal alternative (most desirable, i.e., minimum value for each criterion) and the second alternative is the anti-ideal alternative (least desirable, i.e., maximum value for each criterion). Equation (7) is used to calculate ideal alternative (AI) for the j^{th} criteria, whereas Equation (8) is used to calculate the anti-ideal alternative (AAI) for the j^{th} criteria.

For the non-beneficial criterion,

$$AI_j = \min x_{ij} \tag{7}$$

$$AAI_j = \max(x_{ij}) \tag{8}$$

Step 8: Normalize the extended decision matrix

In this step, the extended matrix is normalized using Equation (9).

For the non-beneficial criterion,

$$n_{ij} = \frac{(x_{AI})_j}{x_{ij}} \tag{9}$$

where n_{ij}= normalized value in MARCOS

Step 9: Construct the weighted normalized matrix

In this step, the weighted normalized matrix is constructed using Equation (10).

$$v_{ij} = n_{ij} \times w_j \tag{10}$$

where v_{ij}= weight normalized value.

Step 10: Calculate the utility function of each alternative

The utility scores for each alternative, idea alternative, and anti-idea alternative are estimated using Equations (11), (12), and (13), respectively.

$$S_i = \sum_{j=1}^{n} v_{ij} \tag{11}$$

$$S_{AI} = \sum_{j=1}^{n} v_{AI,j} \tag{12}$$

$$S_{AAI} = \sum_{j=1}^{n} v_{AAI,j} \tag{13}$$

where S_i= Utility score of alternative i, S_{AI}= Utility score of the idea alternative, and S_{AAI}= Utility score of the anti-idea alternative.

Step 11: Determine the utility degrees

In this step, utility level corresponding to anti-ideal alternative and ideal alternative were estimated using Equation (14) and Equation (15), respectively.

$$K_i^- = \frac{S_i}{S_{AAI}} \tag{14}$$

$$K_i^+ = \frac{S_i}{S_{AI}} \tag{15}$$

where K_i^-= utility level corresponding to the anti- ideal alternative, and K_i^+= utility level corresponding to the ideal alternative

Step 12: Calculate the overall utility function

The overall utility function is calculated using Equation (16).

$$f(K_i) = \frac{K_i^+ + K_i^-}{1 + \frac{1-K_i^+}{K_i^+} + \frac{1-K_i^-}{K_i^-}} \tag{16}$$

where $f(K_i)$ = Final utility value of ithalternative, $f(K_i^+) = \frac{K_i^+}{K_i^+ + K_i^-}$ and $f(K_i^-) = \frac{K_i^-}{K_i^+ + K_i^-}$

Step 13: Rank estimation

The alternatives are ranked from highest to lowest based on the final utility value. The alternative with the maximum utility value is selected as the optimal parameter setting. The step-by-step calculations are presented in Section 4.1.

2.2. Desirability Approach

Desirability analysis is employed to identify the optimal input conditions to get the optimal response outcomes. Initially, each experimental response is converted into an individual desirability value(d_i) using the smaller-the-better criterion, as expressed in Equation (17). Subsequently, the individual desirability indices are combined to calculate the composite desirability using Equation (18). For estimating CD, equal weight for each response was considered. The experimental condition yielding the highest CD value is assigned rank 1 and considered optimal among the tested conditions. The corresponding response values represent the optimal results under the selected experimental conditions. The calculated individual desirability values, composite desirability (CD) values, and corresponding ranks are presented in Section 4.2.

$$d_i = \frac{x_{max} - x_i}{x_{max} - x_{min}} \tag{17}$$

where d_i is individual desirability value, $x_i$is measured response in a particular experimental run. x_{max} and x_{min} are maximum and minimum value for each response.

$$CD = \left(d_{Ra} \times d_T \times d_{VBc} \times d_{Cp}\right)^{1/4} \tag{18}$$

3. Results and Discussion

The measured data obtained under each experimental setting of the Taguchi L_{18} orthogonal array for all responses are reported in Table 1.

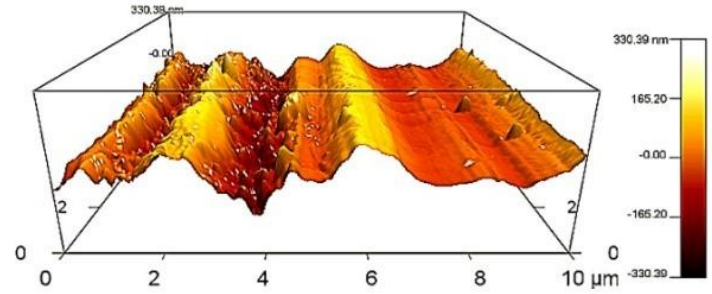
Table 1. Experimentally measured response data.

Run	Input Variables				Measured Responses			
	Tt	*v* (m/min)	*f* (mm/rev)	*d* (mm)	*Ra* (μm)	*T* (°C)	*VB* (mm)	*Cp* (kW)
1	T1	80	0.06	0.1	0.572	148.6	0.037	0.411
2	T1	140	0.12	0.2	0.996	269.2	0.058	0.586
3	T1	200	0.18	0.3	1.399	355.9	0.101	0.794
4	T2	80	0.06	0.2	0.420	136.5	0.033	0.366
5	T2	140	0.12	0.3	0.845	236.3	0.051	0.556
6	T2	200	0.18	0.1	1.132	266.1	0.089	0.661
7	T3	80	0.12	0.1	0.84	105.3	0.028	0.433
8	T3	140	0.18	0.2	1.091	256.8	0.063	0.592
9	T3	200	0.06	0.3	0.745	282.4	0.070	0.733
10	T1	80	0.18	0.3	1.264	233.7	0.062	0.524
11	T1	140	0.06	0.1	0.625	247.1	0.044	0.601
12	T1	200	0.12	0.2	1.176	317.6	0.082	0.741
13	T2	80	0.12	0.3	0.845	174.2	0.047	0.441
14	T2	140	0.18	0.1	1.027	199.3	0.076	0.508
15	T2	200	0.06	0.2	0.503	274.1	0.065	0.642
16	T3	80	0.18	0.2	1.134	175.8	0.050	0.465
17	T3	140	0.06	0.3	0.659	244.8	0.041	0.544
18	T3	200	0.12	0.1	1.09	230.8	0.066	0.678

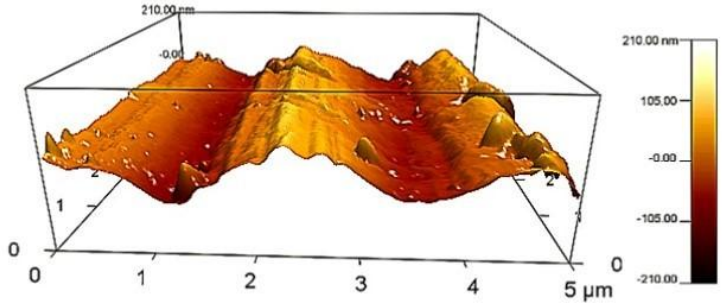
3.1. Surface-Roughness Assessment

The experimental results indicate that surface roughness varies considerably with the tool type (textured and untextured) and cutting parameters. The measured *Ra* values range from 0.420 to 1.399 μm, indicating the strong influence of the selected machining variables. The minimum surface roughness of 0.420 μm was obtained when machining with the T2 tool (groove pattern) at a cutting speed of 80 m/min, a feed rate of 0.06 mm/rev, and a depth of cut of 0.2 mm. This superior surface finish can be attributed primarily to the low feed rate, which reduces the height of feed marks and consequently improves the surface quality [32,33]. The relatively low cutting speed minimizes excessive heat generation and promotes stable cutting, while the moderate depth-of-cut limits cutting forces and tool deflection. In addition, the groove-textured tool (T2) may provide a comparatively stable tool–workpiece interaction, reducing vibration and chatter during machining. The combined effect of these parameters contributes to the lowest surface roughness [34]. The maximum roughness of 1.399 μm was obtained when machining with the untextured tool (T1) maximum cutting speed of 200 m/min, a feed rate of 0.18 mm/rev, and a depth of cut of 0.3 mm. The high feed rate increases the height of feed marks and cutting forces, while the higher cutting speed increases frictional heat generation and tool wear, thereby contributing to increased surface roughness [35,36]. In addition, the low thermal conductivity and high chemical affinity of the titanium alloy may promote heat accumulation, adhesion, and tool wear, resulting in deterioration of surface quality. The absence of surface texturing on the tool may further enhance friction at the tool–workpiece interface and reduce the efficiency of chip flow, consequently leading to poor surface quality [36].

The atomic force microscopy (AFM) topographies reveal distinct differences in the surface topography of runs 3 and 4. Run 3 exhibits pronounced peaks, deep valleys, and substantial height variations, indicating an irregular and highly textured surface, as shown in Figure 5. These variations in surface height reflect non-uniform material removal and contribute to higher surface roughness [37]. In contrast, run 4 presents a comparatively smooth and uniform topography, with fewer prominent asperities and reduced height fluctuations. This indicates more consistent material removal and smaller deviations from the mean surface plane, resulting in the lowest surface roughness. Therefore, the AFM observations are consistent with the measured roughness values, confirming that variations in surface height strongly influence the resulting surface quality. Similar observations have been reported by Waikar and GO [38].



(a) Run 3



(b) Run 4

Figure 5.AFM 3D surface topography of finished surface obtained in (**a**) run 3 and (**b**) run 4.

The XRD patterns of runs 3 and 4 (Figure 6) exhibit similar diffraction peaks at approximately 38–41°, 53–54°, 71°, and 78°,suggesting that the principal crystalline structure of the Ti-grade-9 alloy remained broadly similar under the two machining conditions. However, the absence of phase transformation cannot be conclusively established from the observed peak positions alone without detailed peak identification and quantitative phase analysis. Slight variations in peak positions and intensities are observed between the two conditions. Run 3, machined using an untextured tool at a cutting speed of 200 m/min, a feed rate of 0.18 mm/rev, and a depth of cut of 0.3 mm, represents the most severe machining condition and exhibits greater variation in the diffraction profile. The higher cutting speed, feed rate, and depth of cut may generate increased cutting forces and heat, which can promote greater near-surface plastic deformation and residual

stress development [39]. However, residual stress cannot be directly quantified from the observed peak variations without appropriate measurements, such as XRD peak-shift analysis using a suitable stress-measurement method. In comparison, run 4 exhibits a comparatively stable diffraction profile. The textured tool, combined with lower levels of the cutting parameters, may promote smoother material removal and reduce mechanical and thermal loading on the machined surface [40].Although the XRD results alone do not establish differences in residual stress or confirm the absence of phase transformations, the observed diffraction patterns, together with the lower measured surface roughness in run 4, are consistent with an improved surface condition under this machining condition.

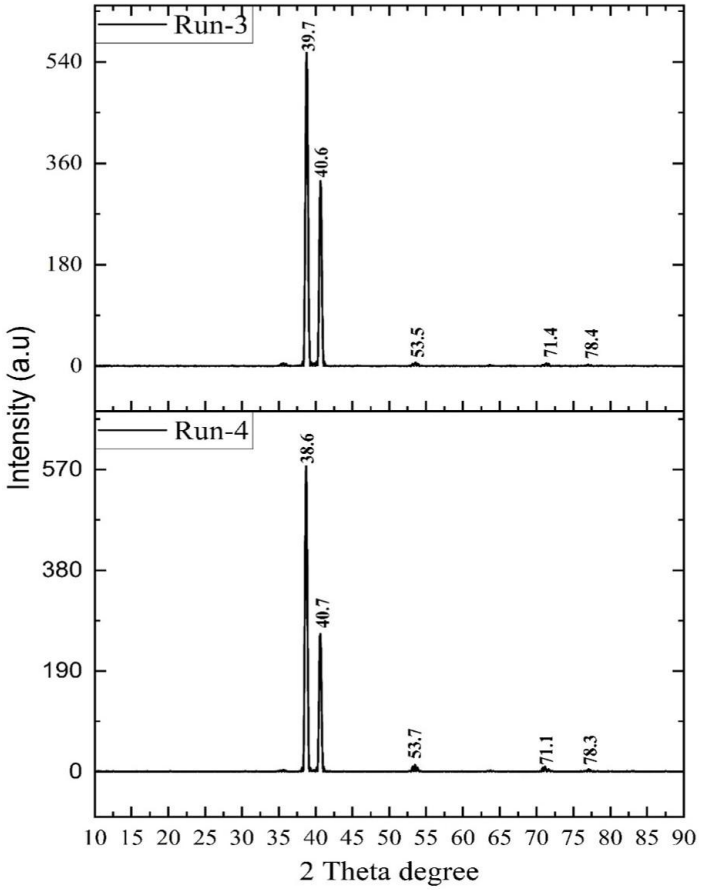


Figure 6. Comparison of XRD results of run 3 and run 4.

The probability plot (Figure 7a) indicates that the experimentally obtained values of surface roughness are approximately normally distributed, as most of the data lie close to the fitted linear line. Furthermore, the *p*-value (0.613) is greater than 0.05, indicating no significant departure from normality. Therefore, it is best suited for statistical assessment. From the main-effects plot (Figure 7b), feed rate has the strongest influence on *Ra* as indicated by the largest variation in the mean. The lowest *Ra* is observed for the grooved tool (T2). The *Ra* was also gradually increased with improving cutting speed and depth of cutting. The interaction plot (Figure 7c) illustrates how the effect of one machining parameter may vary with the level of another parameter. The non-parallel and crossing lines provide qualitative indications of possible interactions between parameter pairs; however, these visual patterns alone do not establish statistical significance. The *Tt–f*, *Tt–d*, and *f–d* pairs appear to exhibit more pronounced interaction trends, as indicated by the noticeable deviations from parallelism and the crossing of lines. Among these pairs, the interaction between *Tt* and *d* exhibited the strongest observed effect on surface roughness. These observations should therefore be interpreted as exploratory indications

of potential interactions, and their statistical significance can only be established through an appropriate statistical test supported by sufficient experimental data.

The surface plot in Figure 8a shows that surface roughness (*Ra*) increases with feed rate at different cutting speeds. The lowest *Ra* is observed at lower feed rates and cutting speeds, whereas higher feed rates produce larger feed marks and greater cutting loads, resulting in increased roughness. The surface plot in Figure 8b shows a relatively low *Ra* in the region corresponding to a lower feed rate and a moderate depth of cut. Roughness increases with feed rate and reaches its highest values at higher feed rates and depths of cut, potentially due to increased cutting forces, deformation, and tool–workpiece interaction. Figure 8c shows only marginal variations in *Ra* with cutting speed and depth of cut. The relatively higher *Ra* observed at low cutting speeds and high depths of cut may be attributed to increased cutting loads and possible material adhesion or built-up edge formation. Figure 8d shows that the interaction between tool type (*Tt*) and cutting speed produces comparatively small changes in *Ra*. The lower cutting speed results in relatively lower *Ra* when the grooved tool (T2) is used for machining. The relatively small slope of the *Ra* response surface suggests that the interaction between tool type and cutting speed is less pronounced than the feed-related interactions shown in Figure 7a,b. Such behavior may arise because tool geometry and cutting-edge conditions affect the contact pattern, material removal mechanism, friction, and formation of feed marks.

The ANOVA was conducted using an additive main-effects model to evaluate the statistical significance of the selected machining parameters. The results (Table 2) indicate that all four factors significantly influence the measured response at the 5% significance level. Feed rate exhibits the highest contribution (80.170%) [41], followed by tool type (10.186%), cutting speed (6.756%), and depth of cut (1.735%). Although depth of cut has a relatively low contribution, its *p*-value of 0.016 indicates a statistically significant main effect under the fitted model. Since interaction effects were not explicitly estimated, the results should be interpreted as the significance of the main effects within the adopted model.

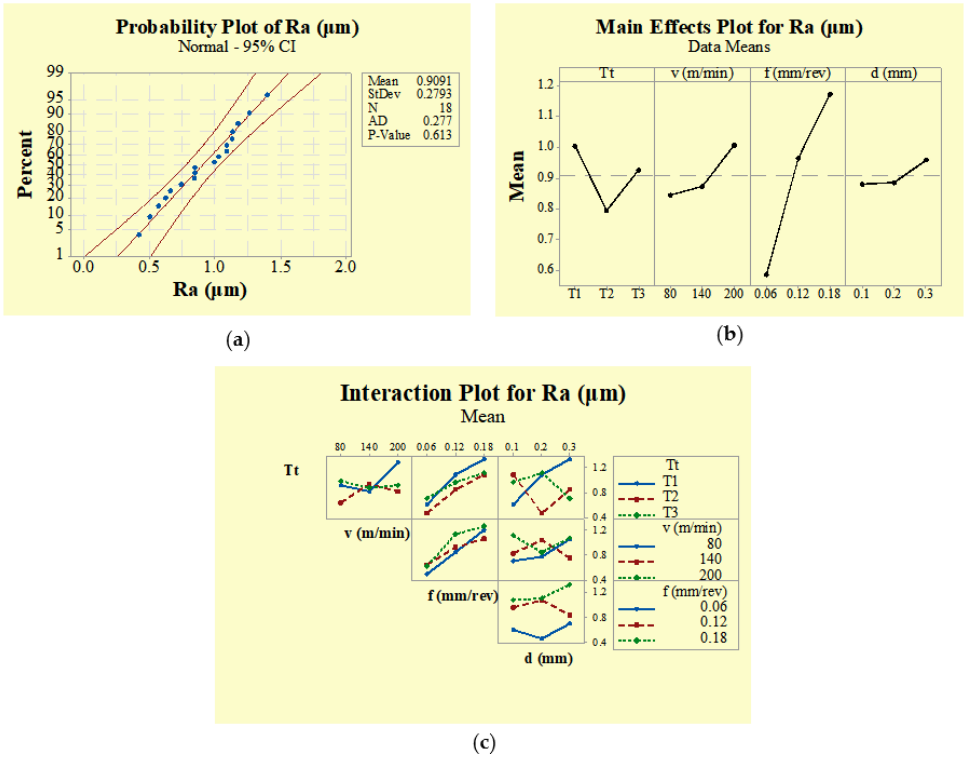


Figure 7. (**a**) Probability plot, (**b**) main-effects plot, and (**c**) interaction plots for response *Ra*.

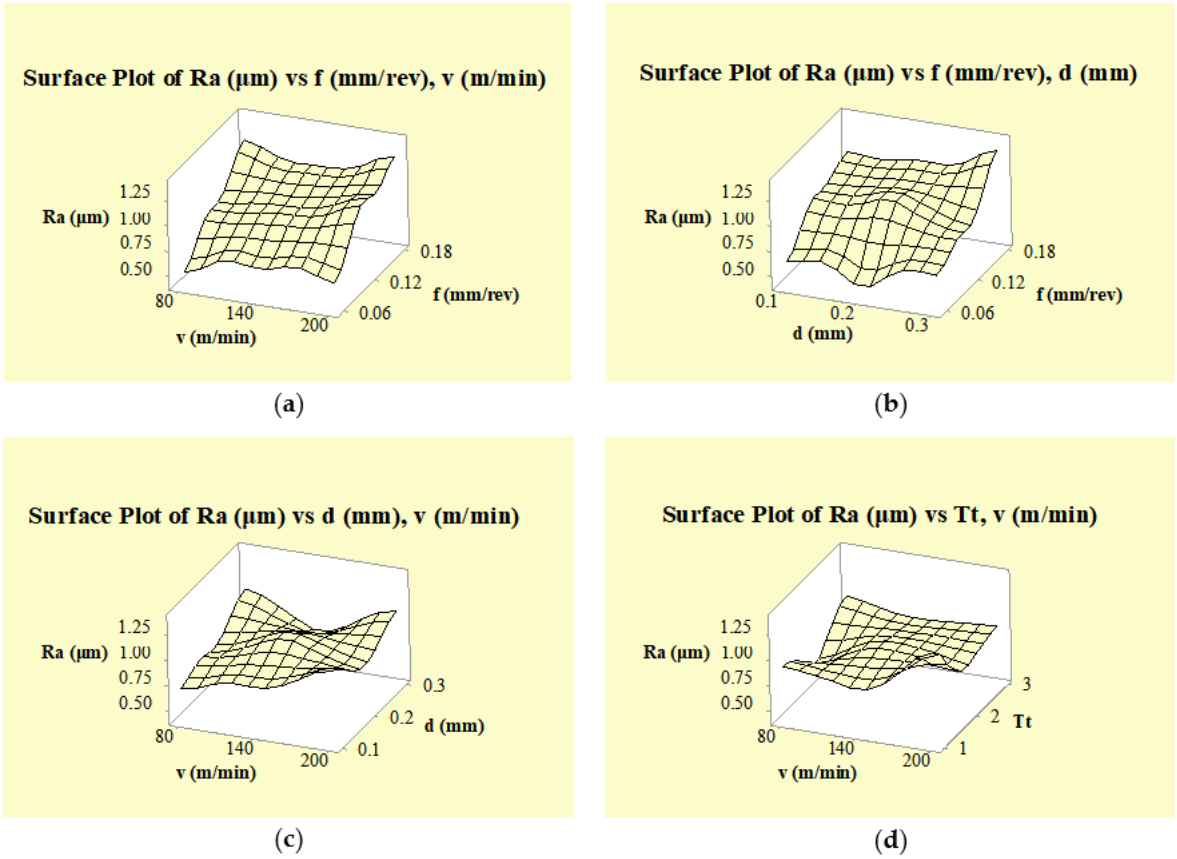


Figure 8. Surface plots for response *Ra* vs (**a**) *f*, *v*; (**b**) *f*, *d*; (**c**) *d*, *v*; (**d**) *Tt*, *v*.

Table 2. ANOVA results for response *Ra*.

Source	DF	Adj SS	Adj MS	F	*p*	Impact (%)	Significant
Tt	2	0.13504	0.06752	39.80	0.000	10.186	Yes
v	2	0.08957	0.04478	26.40	0.000	6.756	Yes
f	2	1.06280	0.53139	313.25	0.000	80.170	Yes
d	2	0.02300	0.01149	6.78	0.016	1.735	Yes
Error	9	0.01527	0.00169				
Total	17	1.32568					

3.2. Cutting-Temperature Analysis

The cutting temperature during dry turning of Ti-grade 9 ranged from 105.3 to 335.9°C across the 18 experimental runs shown in Table 1 and Figure 9. The maximum temperature of 355.9°C was recorded with the untextured carbide tool (T1) at a cutting speed of 200 m/min, a feed rate of 0.18 mm/rev, and a depth-of-cut of 0.3 mm. This high temperature can be attributed to the combined effect of increased cutting variables, which intensify plastic deformation, friction, and cutting forces in the machining zone. The relatively low thermal conductivity of Ti-alloys restricts heat dissipation, resulting in greater heat accumulation near the tool-workpiece interface [42]. In contrast, the minimum temperature of 105.3°C was obtained using the dotted-pattern tool (T3) at 80 m/min, 0.12 mm/rev, and 0.1 mm depth of cut. The lower temperature associated with T3 can be attributed to the interrupted tool–chip contact generated by the dotted pattern. This can reduce the effective contact area and frictional resistance and facilitate chip movement. The groove tool (T2) also exhibited lower temperatures than the untextured tool under several cutting conditions, indicating the beneficial role of surface texturing in modifying tool-chip contact and reducing heat generation [42]. Considering average

temperatures for each tool, the untextured tool (T1) produced about 22–23% higher temperatures than the textured tool. A similar observation was reported by Wu et al. [43].

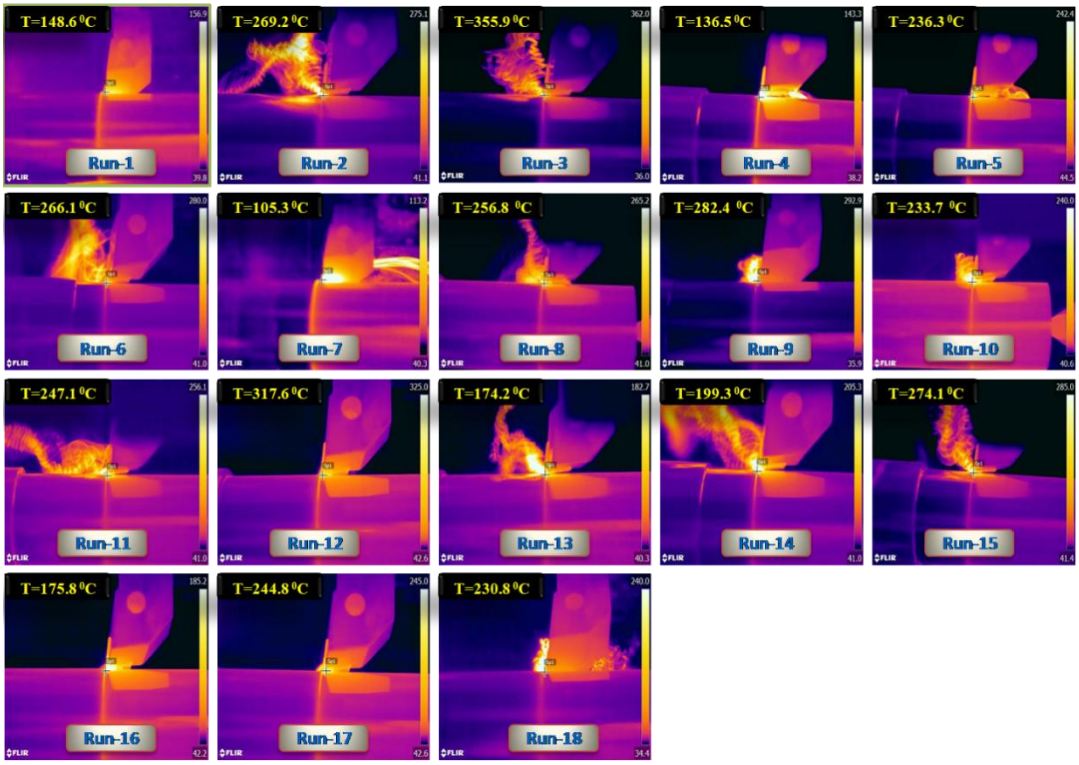


Figure 9. FLIR thermal images showing temperature variation for each experimental run.

The normal probability plot (Figure 10a) indicates that the measured cutting temperature data approximately follows a normal distribution. The fitted points lie reasonably close to the straight reference line. Additionally, the *p*-value exceeds 0.05, indicating that the data are well-suited for statistical analysis. The main-effects plot (Figure 10b) indicates that cutting speed has the strongest impact on cutting temperature, with the mean temperature increasing from 162.35°C at 80 m/min to 287.82°C at 200 m/min. This increase is attributed to enhanced plastic deformation and frictional heat generation at higher cutting speeds. The mean temperature for T1 (untextured tool) was highest (262.02°C), whereas T2 (grooved) and T3 (dotted) tools showed lower temperatures of 214.42°C and 215.98°C, respectively, indicating the beneficial thermal effect of surface texturing. Increasing the depth of cut also increased temperature due to higher material removal load, while a feed rate greater than 0.12 mm/rev showed a sharp increase in temperature due to the increased uncut chip thickness, material removal rate, and cutting forces, which improve plastic deformation and frictional heat generation at the tool–chip interface [44,45]. The interaction plot (Figure 7c) illustrates how the effect of one machining parameter may vary with the level of another parameter. The non-parallel and crossing lines provide qualitative indications of possible interactions between parameter pairs; however, these visual patterns alone do not establish statistical significance. The *Tt–f*, *Tt–d*, and *f–d* pairs appear to exhibit more pronounced interaction trends, as indicated by the noticeable deviations from parallelism and the crossing of lines. The interaction between *Tt* and *d* exhibited a stronger observed effect on cutting temperature than the other factor pairs. These observations should therefore be interpreted as exploratory indications of potential interactions, and their statistical significance can only be established through an appropriate statistical test supported by sufficient experimental data.

From Figure 11a, cutting temperature exhibits a steep upward trend as cutting speed increases from 80 to 200 m/min due to high deformation rates and intense frictional heating at the tool–chip contact zone. Increasing feed value from 0.06 to 0.18 mm/rev further escalates thermal generation due to the increased chip cross-sectional area and higher cutting loading. Similarly, from Figure 11b, the simultaneous increase of feed and depth of cut leads to an increase in cutting temperature due to the increased contact area of the uncut chip and tool. Moreover, the middle zones of the surface plot display moderate non-linear variations, indicating that local thermal equilibrium changes and tool heat-dissipation geometry balance the increased material removal rate. From Figure 11c, a diagonal rise in temperature was observed when cutting speed and depth of cut were increased together. With increasing depth of cut, the temperature rises less steeply compared to speed increment due to high friction and cutting load generation with growing speed. From Figure 11d, the highest temperature was found to be on the untextured tool at the highest cutting speed. The superior thermal performance of the textured tools is attributed to a reduction in the actual chip-tool contact area and friction coefficient [46]. Moreover, due to reduced real contact area and decreased friction coefficient, the tools with texturing pattern performed better than the untextured tool.

The ANOVA results (Table 3) indicate that all four machining parameters significantly influence the measured response at the 5% significance level. Cutting speed exhibits the highest contribution (68.913%), followed by depth of cut (13.654%), tool type (12.492%), and feed rate (3.758%). Although feed rate has a considerably lower contribution than cutting speed, its *p*-value of 0.002 confirms a statistically significant main effect within the adopted ANOVA model. Therefore, the contribution percentage indicates the relative magnitude of each factor's influence, whereas the *p*-value indicates the statistical evidence against the null hypothesis of no main effect.

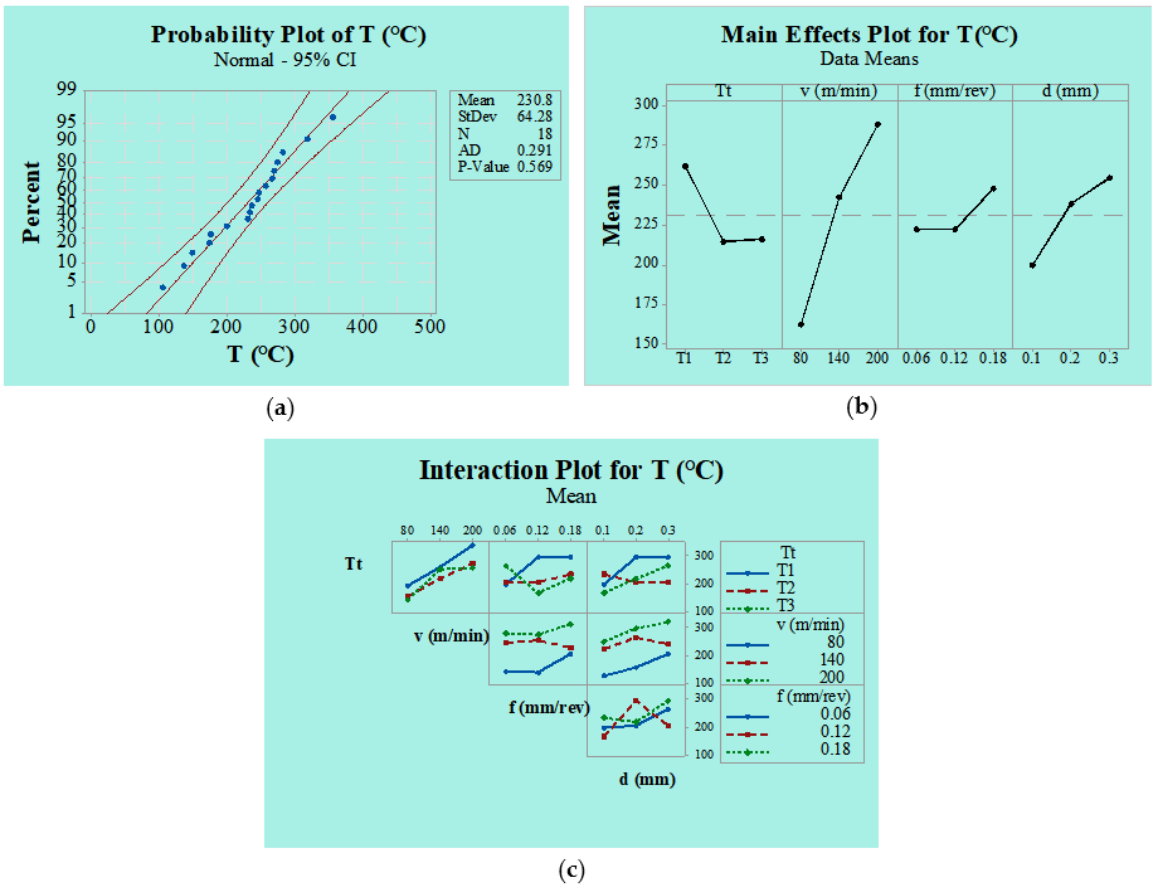


Figure 10. (**a**) Probability plot, (**b**) main-effects plot, and (**c**) interaction plots for response *T*.

https://doi.org/10.3390/mi17111264

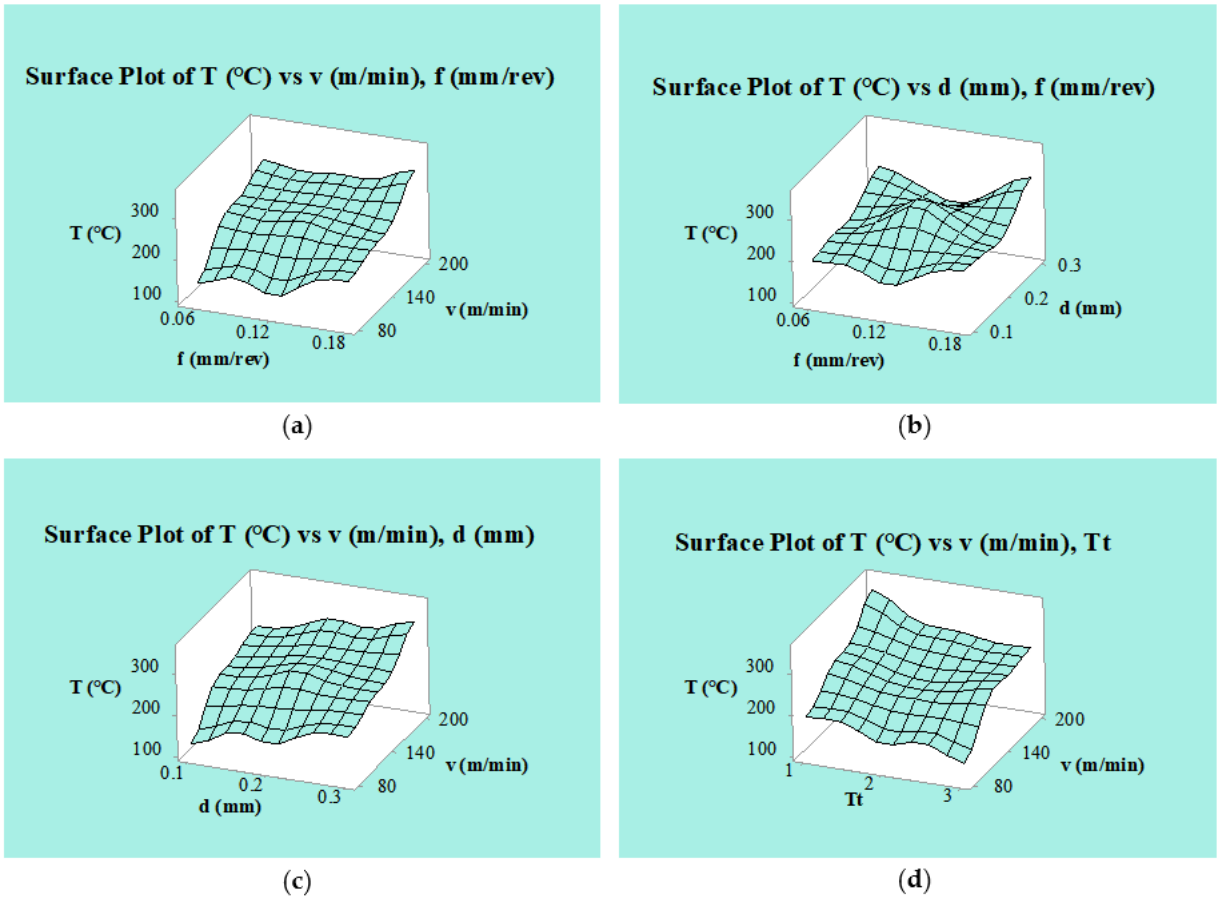


Figure 11. Surface plots for response *T* vs (**a**) *f* , *v*; (**b**) *f*, *d*; (**c**) *d*, *v*; (**d**) *Tt*, *v*.

Table 3. ANOVA results for response *T*.

Source	DF	Adj SS	Adj MS	F	*p*	Impact (%)	Significant
Tt	2	8774.6	4387.3	47.61	0.000	12.492	Yes
v	2	48,404.4	24,202.2	262.64	0.000	68.913	Yes
f	2	2640.2	1320.1	14.33	0.002	3.758	Yes
d	2	9590.5	4785.3	52.04	0.000	13.654	Yes
Error	9	829.3	92.1				
Total	17	70,239.1					

3.3. Flank-Wear Assessment

Figure 12 illustrates the optical micrographs of flank wear (*VB*) across the 18 experimental runs during dry turning of Ti-grade-9 alloy. The observed wear values range from a minimum of *VB* = 0.028 mm (run 7) to a maximum of *VB* = 0.101 mm (run 3), demonstrating clear variations based on the combined effects of process variables and tool-surface textures. The maximum wear (0.101 mm) was produced with the untextured tool at the highest levels of cutting speed (200 m/min), feed (0.18 mm/rev), and depth of cut (0.3 mm). Under these aggressive conditions, the untextured tool yielded the highest wear due to the generation of elevated cutting temperatures (355.9°C). The low thermal conductivity of Ti-grade 9 (6.7 W/mK) caused approximately 80% of total generated heat to remain in the cutting zone [47], leading to thermal softening of the tool and severe edge loss, as shown in Figure12 (Run 3). The minimum flank wear of 0.028 mm corresponds to run 7 with the T3 tool, rather than the grooved T2 tool. However, when the average flank-wear values obtained for the respective tool types are considered, the T2 tool exhibited better overall wear performance than the T3 tool. Reducing the cutting

speed to 80 m/min and the depth of cut to 0.1 mm may have reduced the strain rate and heat generation, resulting in lower flank wear. Furthermore, the grooved pattern disrupted continuous tool–chip contact, drastically reducing the intimate contact area and normal contact stress, thereby minimizing heat generation and delaying wear progression [48]. Untextured tools experienced greater thermal and mechanical damage, resulting in higher wear rates than both textured tools. Micro-textured tools act as micro-reservoirs for debris entrapment, reduce the intimate contact area, and lower the friction coefficient. This mitigates temperature accumulation and prevents rapid progression of flank wear.

The microscopic observations (Figure 12) revealed a relatively uniform wear land with parallel abrasive marks or fine grooves along the cutting direction. The interaction between hard constituents (alpha-phase) present in the workpiece and the tool tip can promote the development of abrasive marks (shining marks) on the tool tip. These marks are clearly visible on each tool; thus, it can be said that abrasive wear was most common in the entire tool-wear study. Severe abrasion was most pronounced at the highest cutting speed conditions. It is also true that along with abrasion, adhesion, and tool-edge chipping were also found in higher levels of cutting conditions. Moreover, the highest feed (0.18 mm/rev) with low and moderate speed also produced severe abrasion, followed by deep grooving and chip adhesion. Cutting-edge loss, breakage, and chipping were found in run 3 and run 12, caused by higher stress concentrations combined with elevated cutting parameters and an untextured tool. Deep groove (notch) wear was observed in runs 10 and 15, along with localized micro-chipping in runs 1 and 11, which occurred primarily due to localized contact stresses, severe mechanical shocks at the tool entry, and work hardening at the depth of the cut line, which is characteristic of dry titanium turning.

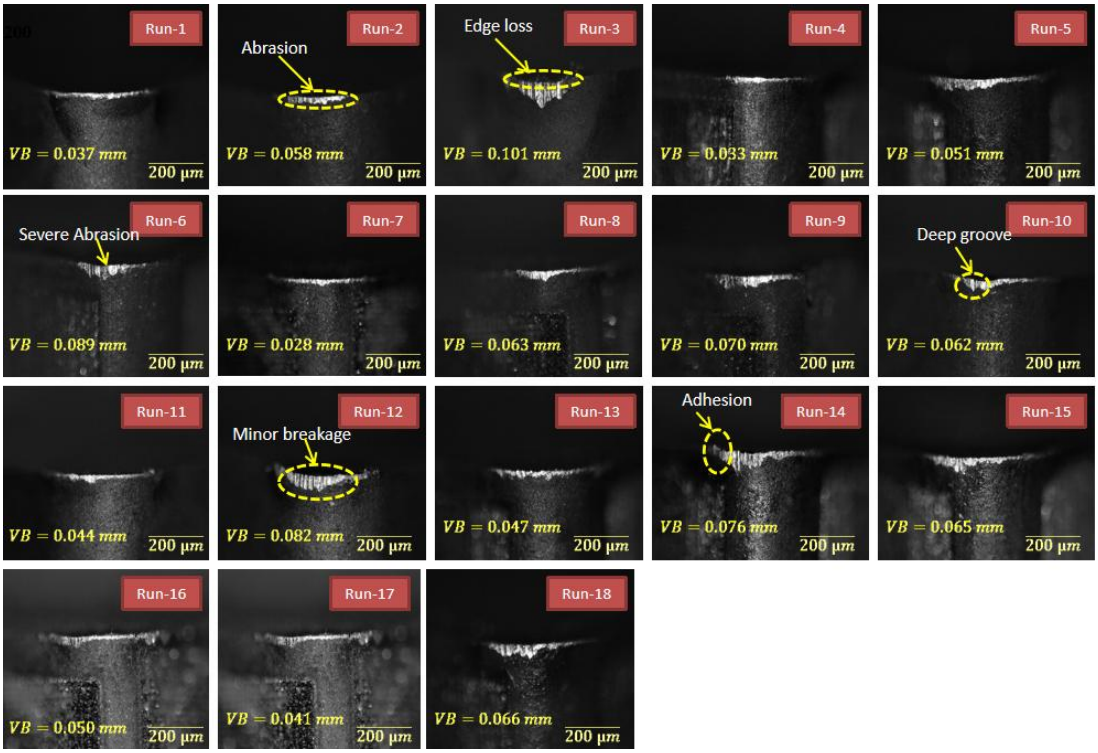


Figure 12. Optical microscopic images of tool flank.

The Raman spectra of the worn cutting tools (Figure 13) show differences in the spectral features observed in runs 3 and 4, suggesting variations in the surface conditions of the worn tools. Run 3, performed using the untextured tool under the highest cutting conditions, exhibited bands at approximately 880, 1160, 1350, and 1580 cm^{-1}. The bands

near 1350 and 1580 cm^{-1} are commonly associated with the D and G bands of carbonaceous materials, respectively. The D band is associated with structural defects and disorder in sp^2-bonded carbon, whereas the G band is related to the in-plane stretching vibrations of sp^2-bonded carbon atoms. The observed bands suggest the presence of carbonaceous material on the worn tool surface. The relatively prominent D-band response in run 3 may indicate a greater degree of structural disorder in this material. However, this interpretation should be considered indicative rather than conclusive. The additional bands near 880 and 1160 cm^{-1} cannot be definitively assigned to specific oxide phases or transferred materials without further spectral analysis and supporting evidence.

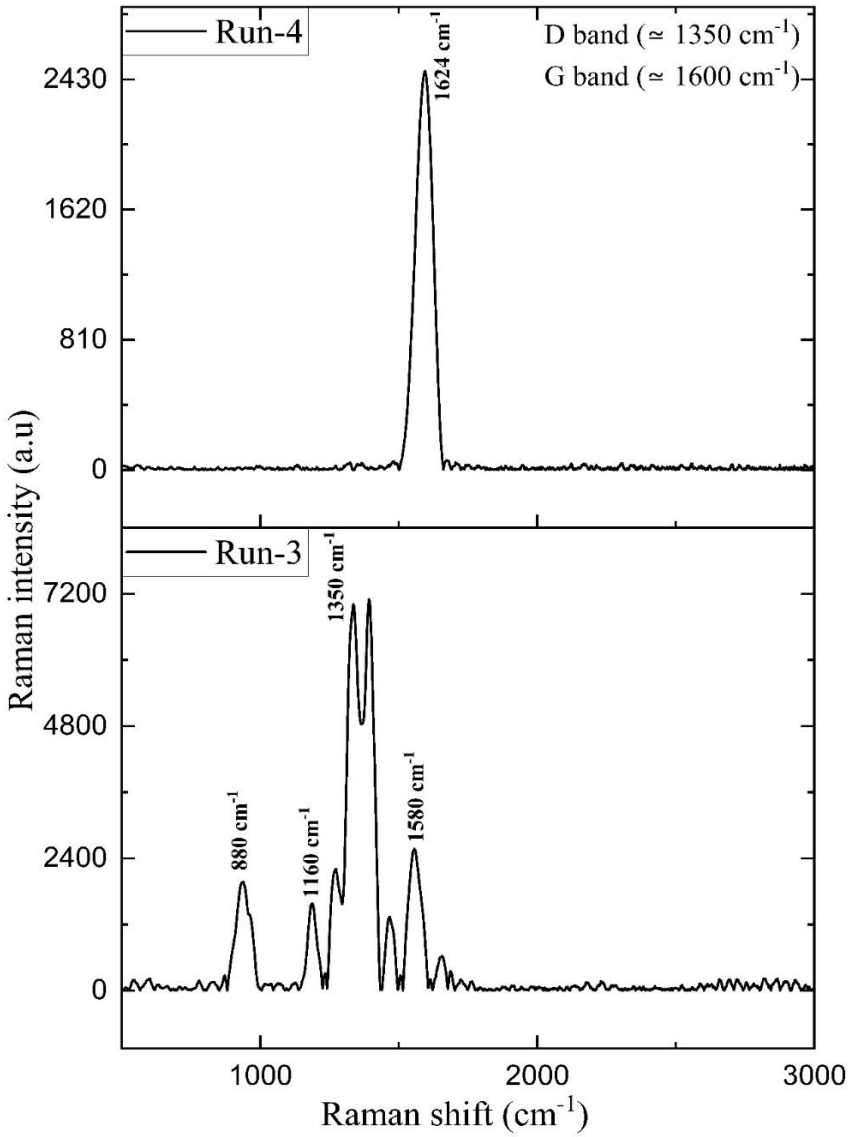


Figure 13. Raman spectra for run 3 and run 4.

In contrast, the spectrum obtained in run 4 showed a dominant feature near 1624 cm^{-1} and a comparatively weaker D-band response. This difference may indicate variations in the structural characteristics or bonding environment of the carbonaceous material formed on the worn tool surface. Under the cutting conditions of run 4, the temperature and contact pressure may promote thermal degradation or transformation of the material present at the tool–chip interface. In combination with the grooved texture, this may help reduce the effective tool–chip contact length and frictional resistance, facilitate debris entrapment, and limit built-up edge (BUE) formation and adhesive interactions.

These effects may contribute to reduced cutting temperature and improved machinability. However, thermal degradation and the associated tribological mechanisms cannot be confirmed from the Raman spectra alone and should be interpreted as possible explanations that require further supporting evidence. Overall, the differences in the Raman spectra, together with the measured tool-wear and cutting-performance results, provide complementary evidence of the different surface conditions and tribological behavior of the grooved-texture tool in run 4 compared with the untextured tool in run 3.

The normal probability plot (Figure14a) shows that the measured-wear data points closely align with the central straight line within a 95% confidence interval,with a *p*-value of 0.948. The high *p*-value confirms that the measured wear values follow a normal distribution, establishing the statistical validity of the experimental results. As depicted in Figure14b, cutting speed exerts the most dominant impact on flank wear progression, evidenced by a sharp rise in average wear as speed increases from 80 to 200 m/min. Higher speeds elevate the plastic deformation rate and thermal generation in the cutting zone. Moreover, due to the poor thermal conductivity of titanium workpiece, generated heat fails to dissipate into the chip and accumulates at the tool, leading to thermal softening and accelerated wear. Furthermore, higher speeds intensify the rubbing action between the tool and the workpiece, producing pronounced abrasive marks on the tool-flank surface. An increase in feed from 0.06 to 0.18 mm/rev significantly escalates flank wear. Larger feed increases the undeformed chip cross-section, which directly elevates normal contact stress. This mechanical loading accelerates two-body abrasion between the hard alpha phase of the workpiece and the tool flank surface. Depth of cut demonstrates the least pronounced effect on flank wear among the process variables. Tool-surface modification via laser texturing demonstrates a steady reduction in average wear from untextured (T1) to grooved (T2) and dotted (T3) tools. This improvement is attributed to the reduced tool–chip contact area, which promotes lower heat generation and minimizes heat accumulation in the cutting zone. As illustrated in the interaction plots (Figure 14c), the *Tt–f*, *Tt–d*, and *f–d* parameter pairs exhibit noticeable deviations from parallelism and, in some cases, intersecting response curves, providing qualitative indications of possible two-factor interactions. In contrast, the remaining parameter combinations exhibit relatively parallel trends, suggesting less pronounced interaction patterns. The interaction between *f* and *d* exhibited the strongest observed effect on flank wear. The trends observed for *Tt–f* and *Tt–d* pairs may be attributed to the combined influence of tool type, feed rate, and depth of cut on flank-wear progression. The wear-mitigating capability of micro-textured tools may vary with the mechanical and thermal loads generated under different cutting conditions. Similarly, feed rate and depth of cutting jointly influence the chip cross-sectional area and may consequently affect contact stresses and localized thermal effects on the cutting tool.

The response surface plots illustrate the combined effects of cutting parameters and tool texturing on flank wear (*VB*), highlighting clear thermo-mechanical interaction dynamics. From Figure 15a, *VB* increases progressively with both parameters, reaching a maximum peak at high cutting speed (200 m/min) and feed rate (0.18 mm/rev) due to intense localized frictional heating and expanded chip cross-sectional areas. In Figure15b, the surface displays a distinct saddle-like curvature, confirming a strong interactive compounding effect where simultaneously high feed and depth of cut drastically elevate normal contact forces and accelerate mechanical rubbing. Conversely, Figure15c demonstrates a dominant upward slope along the cutting speed axis with a relatively gentle slope along depth of cut, confirming that speed induced thermal softening governs wear growth more than cut depth. Finally, Figure15d shows a steep wear inclination for the untextured tool (T1) at elevated speeds, whereas the surface flattens significantly towards the dotted micro-textured tool (T3), con-

firming that micro-textures effectively suppress speed-driven thermal degradation by reducing real tool–chip contact area and lowering friction.

According to ANOVA results (Table 4), cutting speed is the most dominant factor governing flank wear, contributing 59.970% to the total variance with the highest F value of 97.78. In actual practice, higher speeds drastically increase the plastic deformation rate and frictional heat generation at the tool–workpiece interface. Because the workpiece exhibits extremely low thermal conductivity, the generated heat fails to dissipate into the chip and accumulates directly in the cutting zone. Furthermore, this heat accelerates thermal softening of the tool at higher speeds, degrading its hot hardness and producing higher tool wear. Feed rate represents the second most influential parameter, contributing 30.284% with an F value of 49.47, followed by tool type (5.547%).The depth of cut was found to be an insignificant factor in tool wear, contributing only 1.199% to the total variation, with a *p*-value greater than 0.05. This indicates that its effect was not statistically significant under the machining conditions investigated.

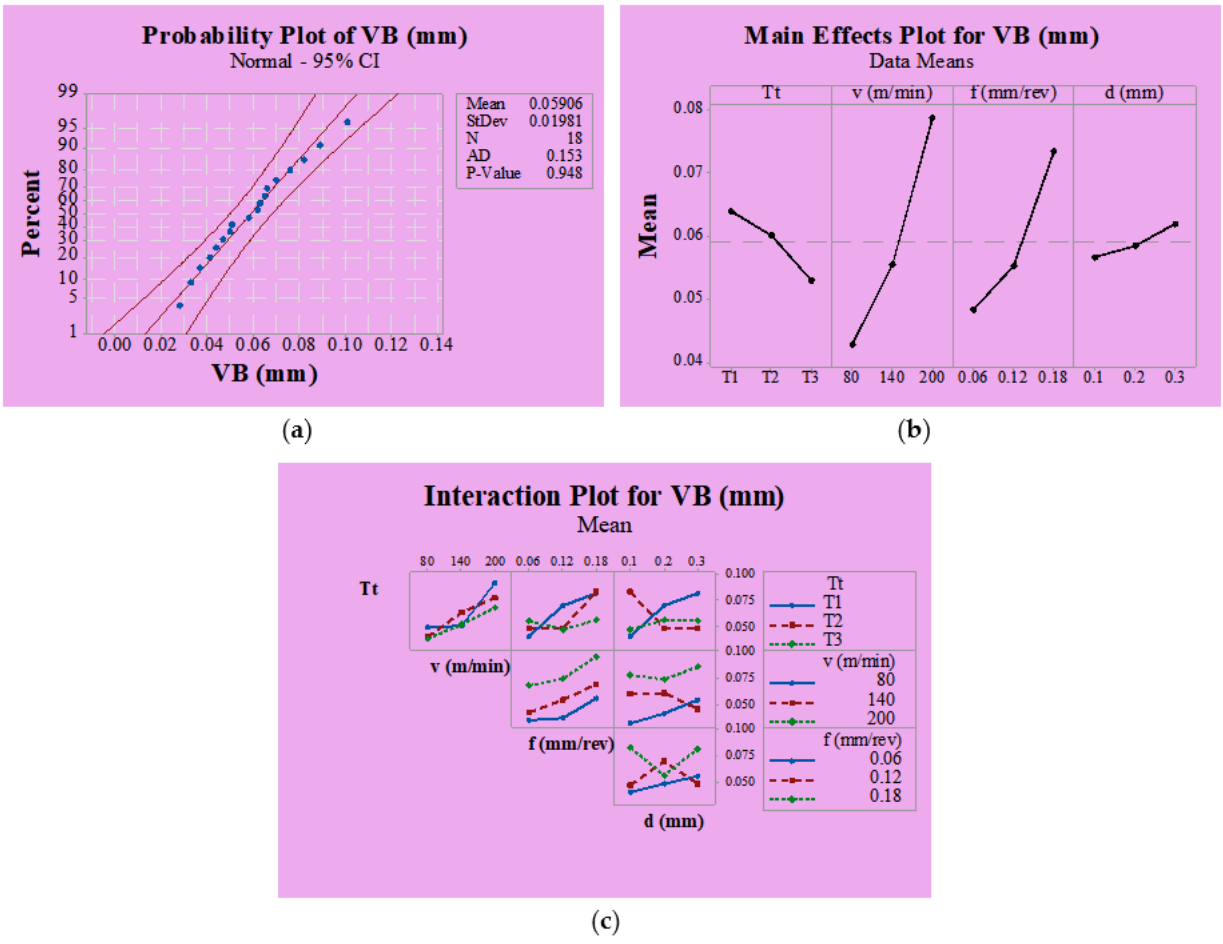


Figure 14. (**a**) Probability plot, (**b**) main-effects plot, and (**c**) interaction plots for response *VB*.

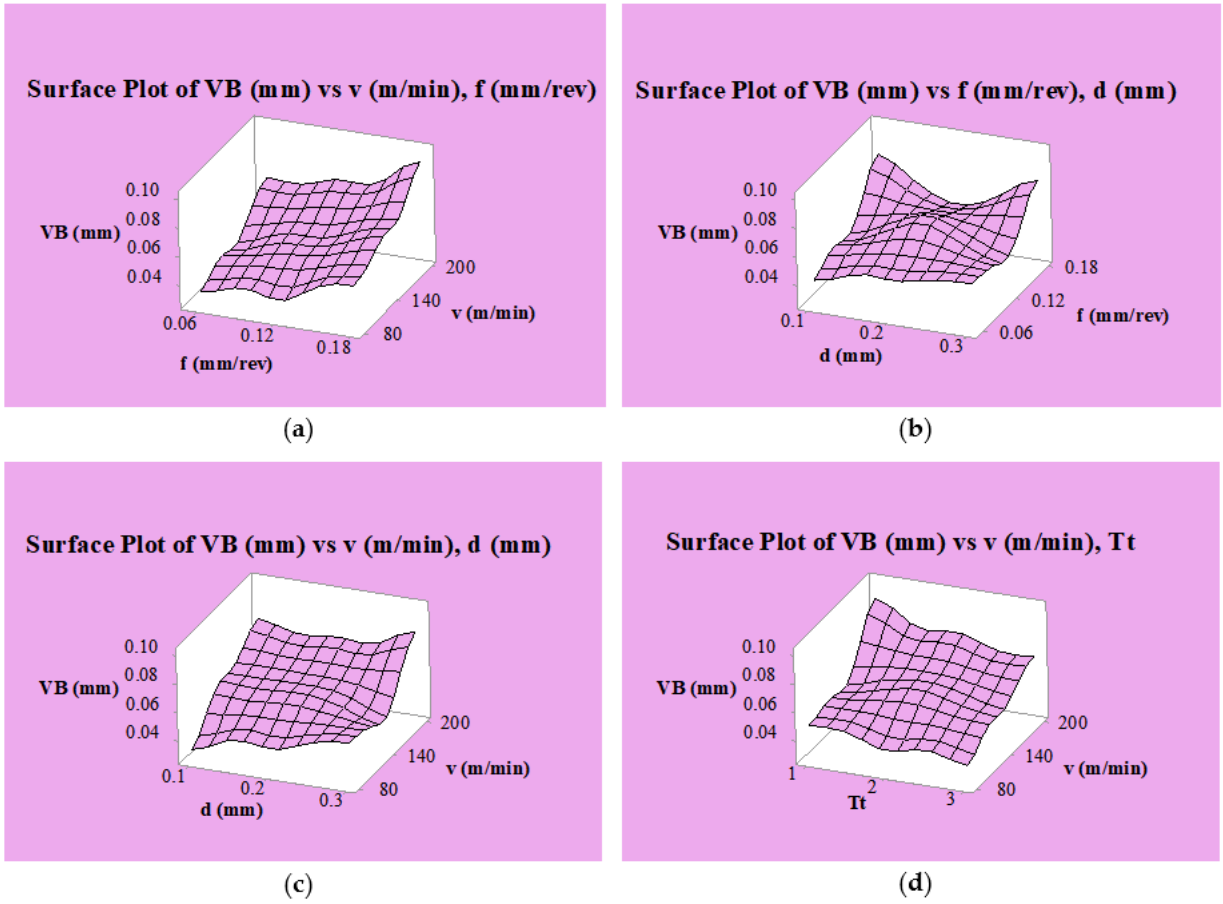


Figure 15. Surface plots for response *VB* vs (**a**) *f*, *v*; (**b**) *d*, *f*; (**c**) *d*, *v*; (**d**) *Tt*, *v*.

Table 4. ANOVA results for response *VB*.

Source	DF	Adj SS	Adj MS	F	*p*	Impact (%)	Significant
Tt	2	0.00037	0.00019	9.14	0.007	5.547	Yes
v	2	0.00400	0.00200	97.78	0.000	59.970	Yes
f	2	0.00202	0.00101	49.47	0.000	30.284	Yes
d	2	0.00008	0.00004	2.15	0.172	1.199	No
Error	9	0.00018	0.00002				
Total	17	0.00667					

3.4. Cutting-Power Assessment

From the experimental data (Table 1), the power consumption during cutting varied from 0.366 to 0.794 kW. The maximum power consumption of 0.794 kW was recorded for the untextured tool (T1) under the most aggressive parameters (v = 200 m/min, f = 0.18 mm/rev, d =0.3 mm). This increase occurs because higher cutting speeds require a higher spindle rotational speed, directly escalating power draw. Additionally, the combined increase in feed and depth of cut expands the undeformed chip cross-section, requiring higher cutting forces to shear the material and further elevating power consumption [49].

The minimum cutting power (0.366 kW) was recorded with the grooved texture tool (T2) at the lowest speed (80 m/min) and feed (0.06 mm/rev) at a moderate depth of cut (0.2 mm). This occurs because operating the cutting process at the lowest speed and feed minimizes the undeformed chip volume and material removal rate, requiring lower shear forces. Furthermore, the grooved texture reduces the actual tool-chip contact length and friction, which significantly can decrease cutting force and overall power consumption [50].

From the probability plot (Figure 16a), the measured power data points are strictly distributed along a straight line and follow the 95% confidence interval, with a *p*-value of 0.966. These outcomes confirmed that the data followed a normal distribution, establishing the statistical validity of the experimental analysis. From Figure 16b, the cutting power increased steeply when cutting speeds increased from 80 to 240 m/min. This is possible because higher spindle speeds and primary shear rates require higher motor power consumption. Moreover, with the rise in feed and depth of cut, the undeformed chip cross-section required higher shear force and power consumption; therefore, power consumption increased with the leading feed and depth of cut. The grooved texture tool produced less average power consumption than the dotted texture and untextured tool. The textured tool reduces power consumption compared to the non-textured tool due to a decrease in tool-chip contact area and friction, thus lowering tool flank wear. The interaction plots (Figure 16c) show noticeable deviations from parallelism for the *Tt–f*, *Tt–d*, and *f–d* parameter pairs, providing qualitative indications of possible interaction effects. These trends suggest that the influence of tool type on cutting power consumption may vary with feed rate and depth of cut. Similarly, the effect of feed rate may depend on the selected depth of cut. Moreover, the interaction between *Tt* and *f*exhibited a stronger observed effect on power consumption than the other factor pairs.However, these interpretations are based solely on the graphical patterns and do not establish the statistical significance of the interactions. Confirmation would require an appropriate statistical test supported by sufficient experimental data.

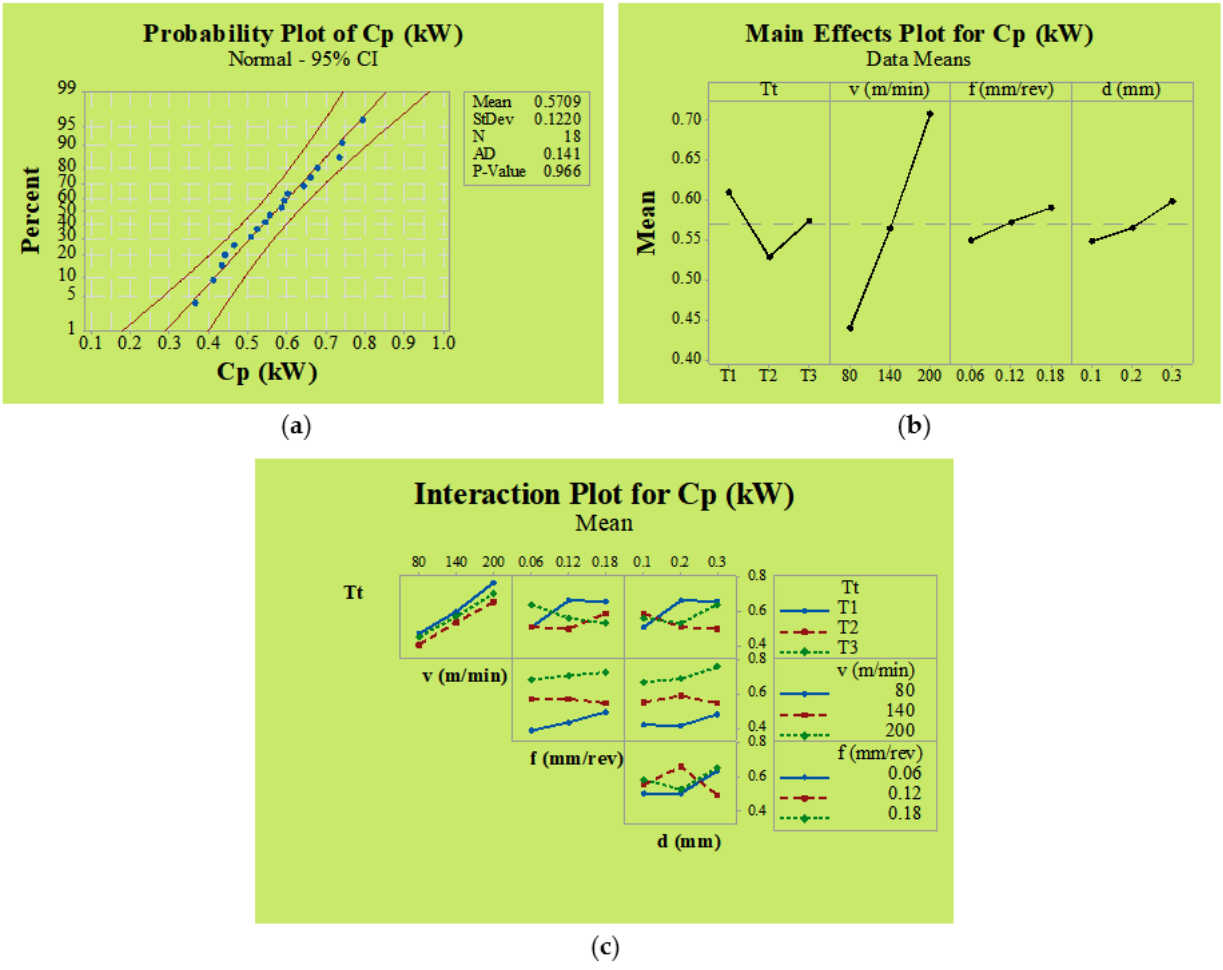


Figure 16. (**a**) Probability plot, (**b**) main-effects plot, and (**c**) interaction plots for response *Cp*.

From the surface plot (Figure 17a), cutting power increased with cutting speed, which was theoretically associated with the relationship cutting force × cutting speed; hence, even if cutting force remained nearly constant, an increase in cutting speed directly increased cutting power. The effect of feed was related to an increase in chip load, which increases the uncut chip thickness and consequently increases the cutting force. Similarly, Figure 17b,c indicate that increasing the depth of cut increased the material cross-sectional area removed, resulting in higher cutting forces and power consumption. Figure 17d shows the influence of tool type (*Tt*), where variations in tool texture modify the tool–chip contact area, friction, chip flow, and shear deformation, thereby altering the cutting force and associated power requirement.

ANOVA (Table 5) indicated that the power consumption was predominantly influenced by cutting speed (85.425%), followed by tool type (7.724%), depth of cut (3.075%), and feed (2.016%). Statistically, based on the *p*-value (<0.05), all the input variables were found to have a significant effect on power consumption. The dominant contribution of cutting speed to cutting-power consumption can be attributed to its strong influence on material removal rate and cutting energy. Tool type also significantly affects power due to variations in tool–chip contact, friction, chip flow, and cutting resistance associated with different tool textures. The contribution of depth of cut is associated with the increased uncut chip cross-sectional area and corresponding cutting force, whereas feed influences power consumption mainly through its effect on chip load and cutting force.

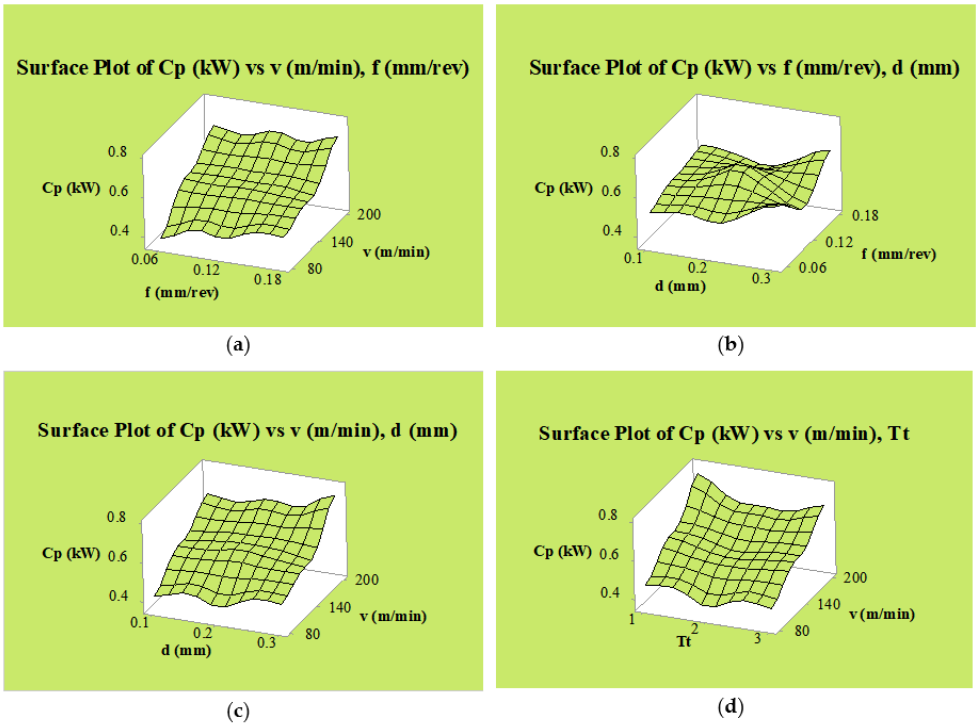


Figure 17. Surface plots for response *Cp* vs (**a**) *f* , *v*; (**b**) *d*, *f*; (**c**) *d*, *v*; (**d**) *Tt*, *v*.

Table 5. ANOVA results for response *Cp*.

Source	DF	Adj SS	Adj MS	F	*p*	Impact (%)	Significant
Tt	2	0.01954	0.00977	19.82	0.001	7.724	Yes
v	2	0.21610	0.10805	219.24	0.000	85.425	Yes
f	2	0.00510	0.00255	5.18	0.032	2.016	Yes
d	2	0.00778	0.00389	7.89	0.010	3.075	Yes
Error	9	0.00443	0.00049				
Total	17	0.25297					

4. Multi-Response Optimization

4.1. CRITIC-MARCOS Hybrid-Optimization Results

The stepwise details of the proposed method are displayed in Section 2.1. Stepwise calculations for CRITIC-based weight estimation are presented in Table 6 (calculated data for Steps 1 and 2) and Table 7 (Calculated data for Steps 3–6). Subsequently, the MARCOS method was applied, and the stepwise calculated results are displayed in Table 8 (calculated data for Steps 7 and 8), Table 9 (calculated data for Steps 9 and 10), and Table 10 (calculated data for Steps 11–13). The highest final utility value was obtained for run 4, which was assigned to the first rank, best-ranked experimental condition among the alternatives investigated. The optimal tool was identified as T2 (grooved pattern on rake and flank surfaces of tool), while the optimal cutting parameters were a cutting speed of 80 m/min, a feed rate of 0.06 mm/rev, and a depth of cut of 0.2 mm. At the optimum condition, the value for response *Ra, T, VB*, and *Cp* was found to be 0.420 µm, 136.5°C, 0.033 mm, and 0.366 kW. These results are in good agreement with previous research on Ti-3Al-2.5V machining, which demonstrated that appropriate optimization of cutting parameters can simultaneously improve surface quality, reduce tool wear and cutting temperature, and the energy requirement of machining [51,52].However, the identified condition represents the best-ranked alternative within the investigated experimental domain and has not been validated beyond the tested range of machining parameters and tool configurations. This limitation should be considered when interpreting the findings and applying them to other machining conditions.

Table 6. Calculated data for decision matrix and normalized matrix for CRITIC method.

Run	Decision Matrix (X_{ij})				Normalized Matrix (N_{ij})			
	Ra	***T***	***VB***	***Cp***	***Ra***	***T***	***VB***	***Cp***
1	0.572	148.6	0.037	0.411	0.845	0.827	0.877	0.895
2	0.996	269.2	0.058	0.586	0.412	0.346	0.589	0.486
3	1.399	355.9	0.101	0.794	0.000	0.000	0.000	0.000
4	0.42	136.5	0.033	0.366	1.000	0.875	0.932	1.000
5	0.845	236.3	0.051	0.556	0.566	0.477	0.685	0.556
6	1.132	266.1	0.089	0.661	0.273	0.358	0.164	0.311
7	0.84	105.3	0.028	0.433	0.571	1.000	1.000	0.843
8	1.091	256.8	0.063	0.592	0.315	0.395	0.521	0.472
9	0.745	282.4	0.07	0.733	0.668	0.293	0.425	0.143
10	1.264	233.7	0.062	0.524	0.138	0.488	0.534	0.631
11	0.625	247.1	0.044	0.601	0.791	0.434	0.781	0.451
12	1.176	317.6	0.082	0.741	0.228	0.153	0.260	0.124
13	0.845	174.2	0.047	0.441	0.566	0.725	0.740	0.825
14	1.027	199.3	0.076	0.508	0.380	0.625	0.342	0.668
15	0.503	274.1	0.065	0.642	0.915	0.326	0.493	0.355
16	1.134	175.8	0.05	0.465	0.271	0.719	0.699	0.769
17	0.659	244.8	0.041	0.544	0.756	0.443	0.822	0.584
18	1.09	230.8	0.066	0.678	0.316	0.499	0.479	0.271
Standard deviation (σ_j)					0.277	0.249	0.264	0.277

Table 7. Estimated correlation coefficient and weight.

	Correlation-Coefficient Matrix (C_{jk})				1-C_{jk}				$\sum$ (1-C_{jk})	ρ_j	W_j
	Ra	***T***	***VB***	***Cp***	***Ra***	***T***	***VB***	***Cp***			
Ra	1	0.448	0.685	0.461	0	0.552	0.315	0.539	1.406	0.389	0.391
T	0.448	1	0.806	0.925	0.552	0	0.194	0.075	0.821	0.204	0.205
VB	0.685	0.806	1	0.817	0.315	0.194	0	0.183	0.692	0.183	0.183
Cp	0.461	0.925	0.817	1	0.539	0.075	0.183	0	0.797	0.221	0.221
									$\sum\rho_j$ =	0.997	

Table 8. Estimated extended decision matrix and normalized matrix.

Run	Extended-Decision Matrix				Normalized Matrix (n_{ij})			
	Ra	***T***	***VB***	***Cp***	***Ra***	***T***	***VB***	***Cp***
AI_j	0.42	105.3	0.028	0.366	1	1	1	1
1	0.572	148.6	0.037	0.411	0.734	0.709	0.757	0.891
2	0.996	269.2	0.058	0.586	0.422	0.391	0.483	0.625
3	1.399	355.9	0.101	0.794	0.300	0.296	0.277	0.461
4	0.42	136.5	0.033	0.366	1.000	0.771	0.848	1.000
5	0.845	236.3	0.051	0.556	0.497	0.446	0.549	0.658
6	1.132	266.1	0.089	0.661	0.371	0.396	0.315	0.554
7	0.84	105.3	0.028	0.433	0.500	1.000	1.000	0.845
8	1.091	256.8	0.063	0.592	0.385	0.410	0.444	0.618
9	0.745	282.4	0.07	0.733	0.564	0.373	0.400	0.499
10	1.264	233.7	0.062	0.524	0.332	0.451	0.452	0.698
11	0.625	247.1	0.044	0.601	0.672	0.426	0.636	0.609
12	1.176	317.6	0.082	0.741	0.357	0.332	0.341	0.494
13	0.845	174.2	0.047	0.441	0.497	0.604	0.596	0.830
14	1.027	199.3	0.076	0.508	0.409	0.528	0.368	0.720
15	0.503	274.1	0.065	0.642	0.835	0.384	0.431	0.570
16	1.134	175.8	0.05	0.465	0.370	0.599	0.560	0.787
17	0.659	244.8	0.041	0.544	0.637	0.430	0.683	0.673
18	1.09	230.8	0.066	0.678	0.385	0.456	0.424	0.540
AAI_j	1.399	355.9	0.101	0.794	0.300	0.296	0.277	0.461

Table 9. Estimated weighted-normalized matrix, and utility score.

Run	Weighted-Normalized Matrix (v_{ij})				(S_i)	(S_{AI})	(S_{AAI})
	Ra	***T***	***VB***	***Cp***			
AI_j	0.391	0.205	0.183	0.221		1	
1	0.287	0.145	0.138	0.197	0.768		
2	0.165	0.080	0.088	0.138	0.471		
3	0.117	0.061	0.051	0.102	0.331		
4	0.391	0.158	0.155	0.221	0.925		
5	0.194	0.091	0.100	0.145	0.532		
6	0.145	0.081	0.058	0.122	0.406		
7	0.196	0.205	0.183	0.187	0.770		
8	0.151	0.084	0.081	0.137	0.453		
9	0.220	0.076	0.073	0.110	0.480		
10	0.130	0.092	0.083	0.154	0.459		
11	0.263	0.087	0.116	0.135	0.601		
12	0.140	0.068	0.062	0.109	0.379		
13	0.194	0.124	0.109	0.183	0.611		

14	0.160	0.108	0.067	0.159	0.495	
15	0.326	0.079	0.079	0.126	0.610	
16	0.145	0.123	0.102	0.174	0.544	
17	0.249	0.088	0.125	0.149	0.611	
18	0.151	0.094	0.078	0.119	0.441	
AAI_j	0.117	0.061	0.051	0.102		0.331

Table 10. Estimated overall utility function and rank.

Run	K_i^+	K_i^-	$f(K_i^+)$	$f(K_i^-)$	$f(K_i)$	Rank
1	0.768	2.319	0.751	0.249	0.709	3
2	0.471	1.424	0.751	0.249	0.436	12
3	0.331	0.999	0.751	0.249	0.305	18
4	0.925	2.796	0.751	0.249	0.855	1
5	0.532	1.606	0.751	0.249	0.491	9
6	0.406	1.227	0.751	0.249	0.375	16
7	0.770	2.327	0.751	0.249	0.712	2
8	0.453	1.367	0.751	0.249	0.418	14
9	0.480	1.451	0.751	0.249	0.444	11
10	0.459	1.388	0.751	0.249	0.424	13
11	0.601	1.816	0.751	0.249	0.555	7
12	0.379	1.146	0.751	0.249	0.350	17
13	0.611	1.845	0.751	0.249	0.564	5
14	0.495	1.495	0.751	0.249	0.457	10
15	0.610	1.843	0.751	0.249	0.564	6
16	0.544	1.644	0.751	0.249	0.503	8
17	0.611	1.846	0.751	0.249	0.565	4
18	0.441	1.333	0.751	0.249	0.408	15

To verify the effectiveness of the identified optimal condition, three independent confirmation experiments were conducted. The average response values for *Ra*, *T*, *VB*, and *Cp* were found to be 0.426 μm, 141.5 °C, 0.032 mm, and 0.361 kW, respectively. These values were close to the corresponding experimental results obtained in run 4 (the original optimal run), indicating good agreement and supporting the reliability of the CRITIC–MARCOS-based hybrid-optimization results under the investigated conditions. The three independent confirmation experiments demonstrated reasonable agreement with the results of the selected experimental condition. However, the final ranking in multi-criteria decision-making may be influenced by the relative weights assigned to the response criteria. Although the CRITIC method provides objective weights based on the statistical characteristics of the observed responses, alternative weighting schemes may produce different rankings. Therefore, sensitivity analysis using alternative weighting methods and a broader experimental design is recommended for future work to assess ranking robustness and explore a wider machining-parameter space.

4.2. Desirability Analysis

To verify the robustness of the multi-response optimization, desirability analysis (DA) was additionally performed and compared with the CRITIC–MARCOS results. As per DA methodology, the individual desirability values, composite desirability (CD) values, and corresponding ranks are calculated and presented in Table 11. The experimental condition with the highest CD value is assigned rank 1 and considered the optimal condition among the tested experimental runs. Experimental run 4 achieved the highest CD value and was therefore identified as the optimal experimental condition (tool type = T2, cutting speed =

80 m/min, feed rate = 0.06 mm/rev and depth of cut = 0.2 mm), providing the most desirable combination of responses under the selected criteria. Both approaches provided the same optimal machining condition, demonstrating consistency between the two optimization techniques. While DA determines the optimum by maximizing the overall desirability of the responses, CRITIC–MARCOS incorporates objective criteria weights and multi-criteria ranking. The agreement between the results strengthens confidence in the selected optimal condition without implying the superiority of either method.

Table 11. Calculated individual desirability values, composite desirability and corresponding ranks.

Run	Individual Desirability (d_i)				Composite Desirability (CD)	Rank
	Ra	*T*	*VB*	*Cp*		
1	0.845	0.827	0.877	0.895	0.860	2
2	0.412	0.346	0.589	0.486	0.449	11
3	0.000	0.000	0.000	0.000	0.000	18
4	1.000	0.875	0.932	1.000	0.950	1
5	0.566	0.477	0.685	0.556	0.566	8
6	0.273	0.358	0.164	0.311	0.266	16
7	0.571	1.000	1.000	0.843	0.833	3
8	0.315	0.395	0.521	0.472	0.418	12
9	0.668	0.293	0.425	0.143	0.330	15
10	0.138	0.488	0.534	0.631	0.388	13
11	0.791	0.434	0.781	0.451	0.590	6
12	0.228	0.153	0.260	0.124	0.183	17
13	0.566	0.725	0.740	0.825	0.707	4
14	0.380	0.625	0.342	0.668	0.483	9
15	0.915	0.326	0.493	0.355	0.478	10
16	0.271	0.719	0.699	0.769	0.569	7
17	0.756	0.443	0.822	0.584	0.633	5
18	0.316	0.499	0.479	0.271	0.378	14

5. Precision Evaluation of the Finished Workpiece Obtained at Optimal Conditions

Precision machining plays a crucial role in sustainable manufacturing by directly influencing product functionality and performance [53]. Circularity and cylindricity are critical geometric tolerances that ensure components meet functional requirements, particularly in applications involving smooth rotation, uniform load distribution, and minimal wear. Tight control of these parameters is essential in aerospace, automotive, and energy industries, where components operate at high speeds and under heavy loads. Errors can cause functional failures, reduced efficiency, and increased maintenance costs. Precision measurement ensures compliance with design tolerances while supporting process optimization, tool-wear monitoring, and quality assistance.

Under the optimal conditions, the circularity and cylindricity errors were measured using a coordinate measuring machine (CMM). The optimized workpiece exhibited circularity and cylindricity errors of 0.014 mm (Figure 18) and 0.026 mm (Figure 19), respectively, with a standard deviation of 0.008 mm. A distinct lobe was observed in the circular profile (Figure 18). According to Denavit-Hartenberg [54], such lobing can result from kinematic and machine tool errors, including tool-position deviations, feed-drive backlash, spindle inaccuracies, guideway error, and insufficient stiffness [54,55]. These effects can cause non-uniform material removal and radial displacement, leading to lobed circularity profiles. Thus, the observed lobing is primarily attributed to inherent errors in the CNC lathe machine tool.

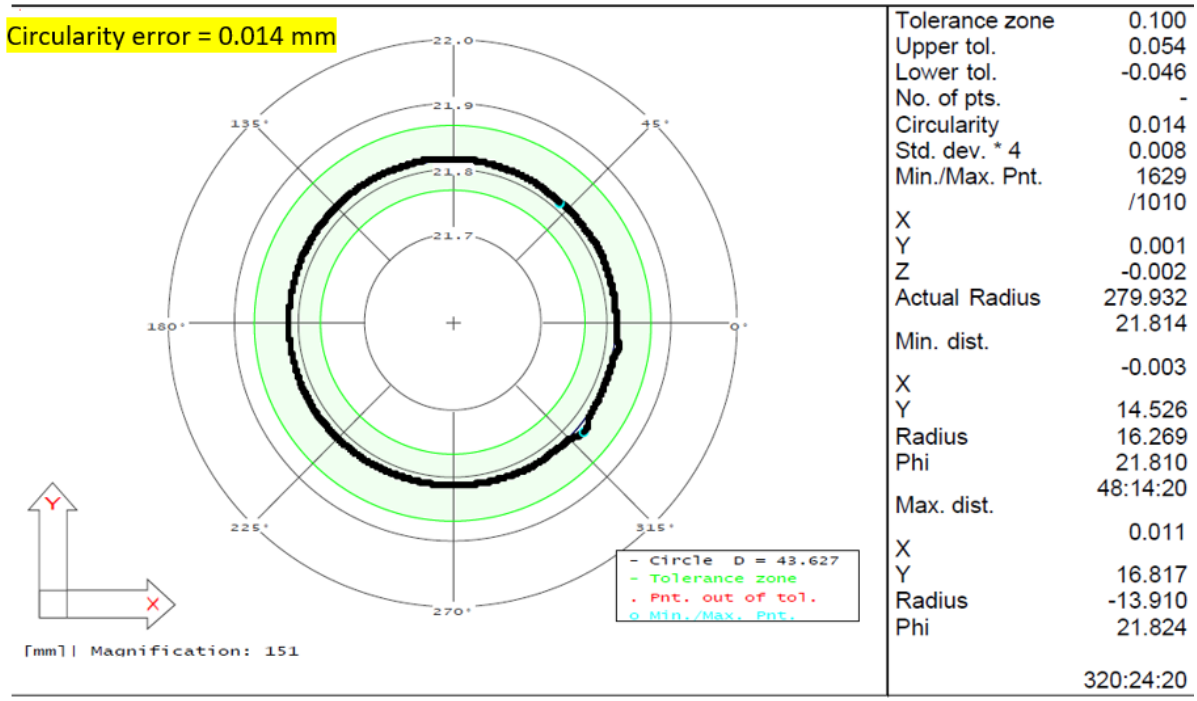


Figure 18. Circularity-error results of finished workpiece obtained at optimal condition.

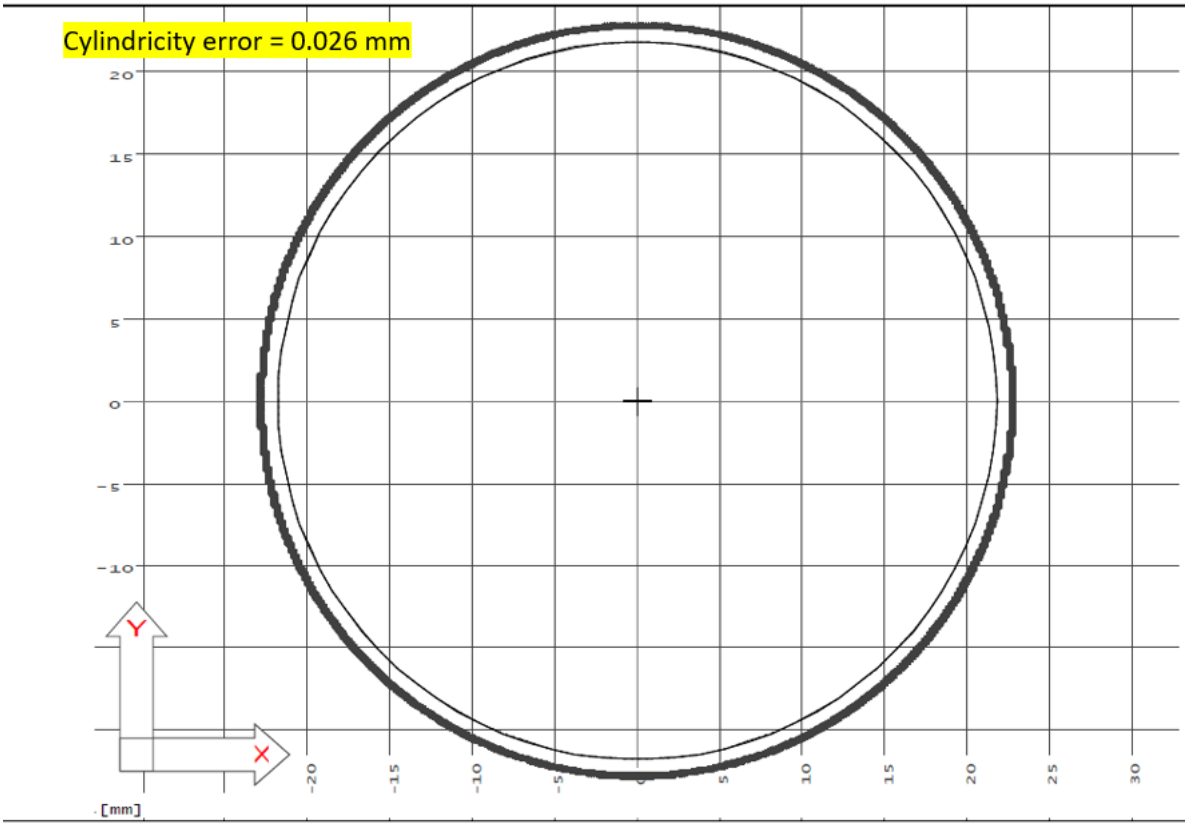


Figure 19. Cylindricity error result of finished workpiece obtained at optimal condition.

https://doi.org/10.3390/mi17111264

6. Conclusions

Based on the experimental findings and analysis, the following key conclusions were drawn from the present study:

- Among the tested conditions, the minimum surface roughness (*Ra*) of 0.420 μm was obtained using tool-type T2 at a cutting speed of 80 m/min, a feed rate of 0.06 mm/rev, and a moderate depth of cut of 0.2 mm. Among the input variables, feed rate had the most pronounced effect on *Ra* (80.170%), followed by tool type, cutting speed, and depth of cut.
- Among the tested conditions, the minimum cutting temperature (*T*) and tool flank wear (*VB*) were obtained using tool-type T3 at a cutting speed of 80 m/min, a moderate feed rate of 0.12 mm/rev, and a minimum depth of cut of 0.1 mm. Among the input variables, cutting speed had the most pronounced effect on both *T* and *VB*, with contributions of 68.913% and 59.970%, respectively.
- Among the tested conditions, abrasion, adhesion, and chipping were identified as the dominating wear mechanism. Abrasive wear was observed in all experimental runs, whereas edge loss due to chipping was predominantly observed at higher cutting speeds when using the untextured tool.
- Among the tested conditions, the minimum power consumption (*Cp*) of 0.366 kW was obtained using tool-type T2, with the lowest cutting speed = 80 m/min, with the lowest feed of 0.06 mm/rev, and moderate depth-of-cut = 0.2 mm. Among the input variables, cutting speed had the greatest effect (77.387%) on Cp followed by tool type, depth of cut, and feed.
- The CRITIC–MARCOS hybrid optimization identified the optimal machining conditions as tool-type T2, a cutting speed of 80 m/min, a feed rate of 0.06 mm/rev, and a depth-of-cut of 0.2 mm. Under these conditions, the optimized response values were *Ra* = 0.420 μm, *T* = 136.5 °C, *VB* = 0.033 mm, and *Cp* = 0.366 kW. These conditions represent the best-ranked alternative within the experimental domain investigated in this study and should not be interpreted as a universal optimum for titanium-alloy machining. Furthermore, although lower feed rates and depths of cut may improve surface finish under certain machining conditions, they can also reduce the material removal rate (*MRR*) and increase machining time. Therefore, the selection of suitable machining parameters should consider the required surface quality and the balance between finishing requirements and productivity. These practical considerations should be considered when applying the findings beyond the scope and limitations of the present investigation.
- The dimensional accuracy of the machined surface was evaluated in terms of circularity and cylindricity errors. The measured circularity and cylindricity errors were 0.014 mm and 0.026 mm, respectively.

Overall, the grooved texture on the rake and flank surfaces of tool T2 exhibited the best overall performance under the selected multi-response optimization criteria within the experimental domain investigated. Accordingly, tool T2 and the associated machining conditions may be considered a promising option for machining titanium alloys under the conditions investigated in this study. However, further validation is required before extending this recommendation to broader industrial applications. Future studies should investigate additional texturing patterns and configurations to establish their influence on machining performance over a wider range of operating conditions. Furthermore, advanced cooling and lubrication techniques, such as minimum-quantity lubrication (MQL), nanofluid-MQL, and cryogenic cooling, could be investigated to improve the machinability of titanium alloys. A systematic investigation of texture geometry, including groove spacing, width, depth, and orientation, is also recommended to

determine how these parameters influence machining performance and multi-response optimization outcomes. Future studies should incorporate replicated machining trials and experimental designs specifically developed to investigate interactions among machining parameters. Such investigations would provide a more robust basis for estimating experimental variability, evaluating interaction effects, and establishing their statistical significance. This would further strengthen the reliability of the statistical analysis and the applicability of the optimized machining conditions. Moreover, future studies could estimate confidence intervals for the main effects, signal-to-noise (S/N) ratio effects of individual control factors, and the combined optimization results.

Author Contributions: Conceptualization A.S. and R.K.; Methodology, A.S. and R.K.; Formal analysis, A.K.S. and A.P.; Investigation, R.K. and A.K.S.; Validation, A.P. and A.K.S.; Writing—Original draft preparation, R.K. and A.S.; Data curation, A.P. and A.K.S.; Writing—review and editing, R.K. and A.K.S.; Supervision, A.K.S. and R.K.; Project administration, A.K.S. and R.K. All authors have read and agreed to the published version of the manuscript.

Funding: No funding received.

Institutional Review Board Statement: Not applicable.

Informed Consent Statement: Not applicable.

Data Availability Statement: The original contributions presented in this study are included in the article. Further inquiries can be directed to the corresponding authors.

Conflicts of Interest: The authors declare no conflicts of interest.

References

1. Yang, D.; Xu, L.; Zhang, Z.; Liu, M.; Liu, B. Review of Microtextured Tools: Pattern Types, Machining Methods, and Cutting Performance. *Int. J. Adv. Manuf. Technol.* **2025**, *141*, 2317–2349.
2. Wojciechowski, S.; Królczyk, G.M.; Maruda, R.W. Advances in Hard–to–Cut Materials Manufacturing, Properties, Process Mechanics, and Evaluation of Surface Integrity. *Materials* **2020**, *13*, 612.
3. Kshitij, P.; Saurav, D. Hot Machining of Difficult-to-Cut Materials: A Review. *Mater. Today Proc.* **2020**, *44*, 2710–2715.
4. Zhang, Z.; Jia, H.; Sun, J. Bioinspired Design of a Ridging Shovel with Anti-Adhesive and Drag Reducing. *Adv. Mech. Eng.* **2015**, *3*, 1–11.
5. Darband, G.B.; Aliofkhazraei, M.; Khorsand, S.; Sokhanvar, S.; Kaboli, A. Science and Engineering of Superhydrophobic Surfaces: Review of Corrosion Resistance, Chemical and Mechanical Stability. *Arab. J. Chem.* **2020**, *13*, 1763–1802.
6. Zhang, Z.; Wang, H.J.; Liang, Y.H.; Li, X.J.; Ren, L.Q.; Cui, Z.Q.; Luo, C. One-Step Fabrication of Robust Superhydrophobic and Super oleophilic Surfaces with Self-Cleaning and Oil/Water Separation Function. *Sci. Rep.* **2018**, *8*, 3869.
7. Pang, K.; Wang, D. Study on the Performances of the Drilling Process of Nickel-Based Superalloy Inconel 718 with Differently Micro-Textured Drilling Tools. *Int. J. Mech. Sci.* **2020**, *180*, 105658.
8. Lu, Y.; Sun, J.; Wu, X.; Chen, F. On-Line Prediction of Impulse Spark and Arc Discharge Removals of Metal Bond in Dry Electrical Discharge Dressing of Diamond Grinding Wheel. *Int. J. Precis. Eng. Manuf.-Green Technol.* **2023**, *10*, 293–310.
9. Zhang, C.; Zou, D.; Mazur, M.; Mo, J.P.; Li, G.; Ding, S. The State of the Art in Machining Additively Manufactured Titanium Alloy Ti-6Al-4V. *Materials* **2023**, *16*, 2583.
10. Kang, K.; Su, S.; Yu, B.; Sun, Z.; Hu, S.; Wang, Z.; Zhao, C.; Wu, L.; Luo, G.; Wei, R. The Review and prospect of Tool Coating Technology. *Int. J. Adv. Manuf. Technol.* **2025**, *137*, 3107–3139.
11. Zhou, Y.; Fu, Y.; Yang, J. Effect of Volcano-Like Textured Coated Tools on Machining of Ti6Al4V: An Experimental and Simulative Investigation. *Int. J. Adv. Manuf. Technol.* **2022**, *120*, 7785–7802.
12. Sristi, N.A.; Zaman, P.B. A Review of Textured Cutting Tools' Impact on Machining Performance from A Tribological Perspective.*Int. J. Adv. Manuf. Technol.* **2024**, *133*, 4023–4057.
13. Grigoriev, S.N.; Okunkova, A.A.; Volosova, M.A.; Hamdy, K.; Metel, A.S. Advances in Texturing of Polycrystalline Diamond Tools in Cutting Hard-to-Cut Materials.*J. Manuf. Mater. Process.* **2026**, *10*, 27.

14. Zhang, J.; Sun, P.; Ali, Q.; Wang, J.; Guo, G.; Li, L.; Hao, X. The Biomimetic Hierarchical Micro-Groove Textured Tool for Enhancing Lubrication and Cooling. *J. Manuf. Process*. **2025**, *155*, 72–81.
15. Garcia-Fernandez, J.; Salguero, J.; Batista, M.; Vazquez-Martinez, J.M.; Del Sol, I. Laser Surface Texturing of Cutting Tools for Improving the Machining of Ti6Al4V: A Review. *Metals* **2024**, *14*, 1422.
16. García-Fernández, J.; Salguero, J.; Vázquez-Martínez, J.M.; del Sol, I.; Batista, M. Influence of Laser Surface Texture Orientation on the Tribological Behaviour of the WC-Co/Ti6Al4V Pair in Dry and Lubricated Conditions. *Wear* **2025**, *571*, 205852.
17. Elias, J.V.; Venkatesh, N.P.; Lawrence, K.D.; Mathew, J. Tool Texturing for Micro-Turning Applications–An Approach Using Mechanical Micro Indentation. *Mater. Manuf. Process.* **2021**, *36*, 84–93.
18. Alok, A.; Kumar, S.; Pandey, S.M.; Kumar, A. Review on the Effect of Surface Textured Tool in the Field of Machining. *Adv. Mater. Process. Technol.* **2024**, *10*, 814–832.
19. Zhang, Y.; Sun, H.; Li, Q.; Sun, K.; Mou, Y.; Zhang, S. Research on the Cutting Performance of Self-Lubricating Tools with Microtexture of the Front and Back Surfaces. *Stroj. Vestn./J. Mech. Eng.* **2025**, *71*, 136–145.
20. Mallikarjuna, P.; Prasanna, P.; Sivaiah, P.; Chengal Reddy, V. MQL Turning Processing of EN24 Alloy Steel Material with Novel Textured Tools. *Mater. Manuf. Process.* **2025**, *40*, 1713–1724.
21. Vijayananth, K.; Pudhupalayam Muthukutti, G.; Keerthiveettil Ramakrishnan, S.; Venkatesan, S.; Zhou, W. An Integrated CRITIC-COPRAS Approach For Multi-Response Optimization on AWJM of Hybrid Filler–Reinforced Polymer Composite and its Surface Integrity.*Int. J. Adv. Manuf. Technol.* **2024**, *131*, 4965–4980.
22. Panigrahi, R.R.; Kumar, R.; Sahoo, A.K.; Panda, A. Optimizing sustainable machining conditions for Incoloy 800HT Using Twin-Nozzle MQL with bio-based groundnut oil lubrication. *Lubricants* **2025**, *13*, 320.
23. Sultana, M.N.; Dhar, N.R. RSM Design-Based Hybrid Approach to Multi-Response Optimization in Milling Ti-6Al-4 V Alloy: A Comparative Study.*Mater. Today Proc.* **2023**, *in press*. https://doi.org/10.1016/j.matpr.2023.03.527.
24. Kavimani, V.; Gopal, P.M.; Ramakrishnan, S.K.; Giri, J.; Alarifi, A.; Sathish, T. Predictive Modelling and Optimization of WEDM Parameter for Mg–Li Alloy Using ANN Integrated CRITIC-WASPAS Approach. *Heliyon* **2024**, *10*,e35194.
25. Uyala, S.B.; Uyala, S.; Jannu, S.; Gadakh, V.S. Multi-Objective Optimization of Machining Parameters for EDM of Magnesium Alloy-Ze41 Using Marcos Algorithm and Different Weighing Methods. SD, CRITIC and MEREC.*Int. J. Adv. Manuf. Technol.* **2024**,*16*, 124.
26. Pradhan, B.B.; Tiwary, A.P.; Masanta, M.; Bhattacharyya, B. Investigation of Micro-Electro-Discharge Machining Process Parameters During Machining of M2 Hardened Die-Steel. *Proc. Inst. Mech. Eng. E J. Process Mech. Eng.* **2024**. https://doi.org/10.1177/09544089241234626.
27. Pendokhare, D.; Kalita, K.; Chakraborty, S.; Čep, R. A Comprehensive Review of Parametric Optimization of Electrical Discharge Machining Processes Using Multi-Criteria Decision-Making Techniques. *Front. Mech. Eng.* **2024**, *10*, 1404116.
28. *ISO 3685:1993*; Tool-Life Testing with Single-Point Turning Tools. International Organization for Standardization (ISO): Geneva, Switzerland, 1993
29. Diakoulaki, D.; Mavrotas, G.; Papayannakis, L. Determining Objective Weights in Multiple Criteria Problems: The Critic Method. *Comput. Oper. Res.* **1995**, *22*, 763–770.
30. Kumari, A.; Acherjee, B. Selection of Non-Conventional Machining Process Using CRITIC-CODAS Method. *Mater. Today Proc*. **2022**, *56*, 66–71.
31. Do, D.T. Multi-Criteria Decision Making Under the MARCOS Method and the Weighting Methods: Applied to Milling, Grinding and Turning Processes. *Manuf. Rev.* **2022**, *9*, 3. https://doi.org/10.1051/mfreview/2022003.
32. Ramesh, S.; Karunamoorthy, L.; Palanikumar, K. Measurement And Analysis of Surface Roughness in Turning of Aerospace Titanium Alloy (Gr5). *Measurement* **2012**, *45*, 1266–1276.
33. Nithyanandam, J.; Das, S.L.; Palanikumar, K. Influence of Cutting Parameters in Machining of Titanium Alloy. *IJST* **2015**, *8*, 556–562.
34. Shastri, A.; Nargundkar, A.; Kulkarni, A.J.; Benedicenti, L. Optimization of Process Parameters for Turning of Titanium Alloy (Grade II) in MQL Environment Using Multi-CI Algorithm. *SN Appl. Sci.* **2021**, *3*, 226.
35. Abdel-Aal, H.A.; Nouari, M.; El Mansori, M.J.T.I. Influence of Thermal Conductivity on Wear when Machining Titanium Alloys. *Tribol.Int.* **2009**, *42*, 359–372.
36. Zheng, K.; Yang, F.; Zhang, N.; Liu, Q.; Jiang, F. Study on the Cutting Performance of Micro Textured Tools on Cutting Ti-6Al-4V Titanium Alloy. *Micromachines* **2020**, *11*, 137.
37. Yang, C.; Dang, C.Q.; Zhu, W.L.; Ju, B.F. High-Speed Atomic Force Microscopy in Ultra-Precision Surface Machining and Measurement: Challenges, Solutions and Opportunities. *Surf. Sci. Technol*. **2023**, *1*, 7.

38. Waikar, R.A.; Guo, Y.B. A Comprehensive Characterization of 3D Surface Topography Induced by Hard Turning versus Grinding. *J. Mater. Process. Technol.* **2008**, *197*, 189–199.
39. Madyira, D.; Laubscher, R.; van Rensburg, N.J.; Henning, P. High speed machining induced residual stresses in Grade 5 titanium alloy. *Proc. Inst. Mech. Eng. Part L J. Mater. Des. Appl.* **2013**, *227*, 208–215. https://doi.org/10.1177/1464420712462319.
40. Yang, S.; Yu, S.; He, C. The Surface Integrity of Titanium Alloy when Using Micro-Textured Ball-End Milling Cutters. *Micromachines* **2018**, *10*, 21.
41. Elshaer, R.N.; El-Aty, A.A.; Sayed, E.M.; Barakat, A.F.; Sobh, A.S. Optimization of Machining Parameters for Turning Operation of Heat-Treated Ti-6Al-3Mo-2Nb-2Sn-2Zr-1.5 Cr Alloy by Taguchi Method. *Sci. Rep.* **2024**, *14*, 16494.
42. Zhang, Y.; Fu, Y.; Li, Q.; Zhang, K.; Liu, K. Study on the Cutting Performance and Remaining Life Prediction of Micro-Texture Ball End Milling Cutters for Titanium Alloys. *Coatings* **2024**, *14*, 814.
43. Wu, Z.; Xing, Y.; Chen, J. Improving the Performance of Micro-textured cutting tools in dry milling of Ti-6Al-4V alloys. *Micromachines* **2021**, *12*, 945.
44. Sun, S.; Brandt, M.; Dargusch, M.S. Characteristics of Cutting Forces and Chip Formation in Machining of Titanium Alloys. *Int. J. Mach. Tools Manuf.* **2009**, *49*, 561–568.
45. Xie, J.; Luo, M.J.; Wu, K.K.; Yang, L.F.; Li, D.H. Experimental Study on Cutting Temperature and Cutting Force in Dry Turning of Titanium Alloy using a Non-Coated Micro-Grooved Tool. *Int. J. Mach. Tools Manuf.* **2013**, *73*, 25–36.
46. He, Y.; Xu, Z.; Li, P.; Liu, M.; Gao, X.; Fan, L. Simulation Study on Cutting Titanium Alloy with Micro- Texture Tool Based on ABAQUS. *LNPU* **2024**, *44*, 61–69.
47. Soori, M.; Karimi Ghaleh Jough, F. Internal Cooling System effects to Heat Transfer and Tool Wear in Turning Operations of Titanium Alloys Ti6Al4V. *TCSME* **2024**, *49*, 118–127.
48. Saraf, G.; Nirala, C.K. Experimental Investigation of Micro-Pillar Textured WC Inserts during Turning of Ti6Al4V under Various Cutting Fluid Strategies. *J. Manuf. Process.* **2024**, *113*, 61–75.
49. Fernández, H.M.; Martín-Béjar, S.; Sevilla Hurtado, L.; Trujillo Vilches, F.J. Optimizing Cutting Parameters for Enhanced Control of Temperature, Cutting Forces, and Energy Consumption in Dry Turning of Ti6Al4V Alloy. *Materials* **2025**, *18*, 942.
50. Agari, S.R.; Lakshmikanthan, A.; Selvan, C.P.; Sekar, K.V. Improvement in the Machining Processes by Micro-Textured Tools During the Turning Process. *Eng. Proc.* **2024**, *61*, 2.
51. Gupta, M.K.; Niesłony, P.; Korkmaz, M.E.; Kuntoğlu, M.; Królczyk, G.M.; Günay, M.; Sarikaya, M. Comparison of Tool Wear, Surface Morphology, Specific Cutting Energy and Cutting Temperature in Machining of Titanium Alloys Under Hybrid and Green Cooling Strategies. *Int. J. Precis. Eng. Manuf. Green Technol.* **2023**, *10*, 1393–1406.
52. Sellappan, S.N.; Chinnappandi, M.; Jeyaraj, P.K.; Seethalakshmi, S.K.S.P.; Sulaiman, Z.; RahimSulaiman, A.R.A. Multi-Objective Optimization of Micromachining Parameters for Titanium Alloy Ti-3Al-2.5 V Using Grey Relational Analysis. *Eng. Proc.* **2025**, *107*, 51.
53. Mallick,R.;Kumar,R.;Panda,A.;Sahoo, A.K.;Sahu,R.;Swain,J.Assessing Hard-Turning Performance Improvement Using Ionic Liquid-Infused Cutting Fluids. Tribological Benefits, Tool Life Assessment, and Sustainable Machining. *Proc. Inst. Mech. Eng. Part C J. Mech. Eng. Sci.* **2025**, *239*, 4555–4580.
54. Lamikiz, A.; López de Lacalle, L.N.; Ocerin, O.; Díez, D.; Maidagan, E. The Denavit and Hartenberg approach applied to evaluate the consequencesinthetooltippositionofgeometricalerrorsinfive-axismilling centres.*Int. J. Adv. Manuf. Technol.* **2008**, *37*, 122–139.
55. Madhu, P.; Rao, S. Interactive Approach in Improving Rigidity of LatheStructure.*Int. J. Interact. Des. Manuf.* **2021**,*15*, 35–45.

Disclaimer/Publisher's Note: The statements, opinions and data contained in all publications are solely those of the individual author(s) and contributor(s) and not of MDPI and/or the editor(s). MDPI and/or the editor(s) disclaim responsibility for any injury to people or property resulting from any ideas, methods, instructions or products referred to in the content.